Carson, B., Westbrook, G.K., Musgrave, R.J., and Suess, E. (Eds.), 1995
Proceedings of the Ocean Drilling Program, Scientific Results, Vol. 146 (Pt. 1)

14. MAGNETIC ANISOTROPY FABRICS FROM THE CASCADIA ACCRETIONARY PRISM[1]

Bernard A. Housen[2] and Takaharu Sato[3]

ABSTRACT

Magnetic anisotropy fabrics were measured in 495 specimens collected from the Cascadia accretionary prism to characterize the development of mineral preferred orientation fabrics during deformation. Comparison of high-field and low-field susceptibilities was used to determine the relative contributions of the paramagnetic clay minerals and the ferrimagnetic trace minerals (magnetite, greigite, pyrrhotite) to the magnetic susceptibility fabrics. Sites 888 and 891 have anisotropy of magnetic susceptibility (AMS) fabrics that are controlled primarily by the ferrimagnetic minerals. Sites 889/890 and 892 have AMS fabrics that are controlled, to varying degrees, by both paramagnetic clays and the ferrimagnetic minerals. Rock magnetic experiments indicate that both magnetite and magnetic sulfides (greigite and/or pyrrhotite) are present in nearly all the specimens. The AMS fabrics from all sites agree well with the observed structures in spite of the complex magnetic mineralogy in these sediments. In particular, Sites 888 and 891 appear to have comparable magnetic mineralogies, along with similar depositional environments, ages, and lithologies. Using Site 888 as an undeformed reference, a weak tectonic fabric overprint is indicated by the Site 891 AMS results.

INTRODUCTION

Magnetic anisotropy measures the preferred orientation of minerals in rocks and sediments and is useful to determine changes in mineral fabrics produced by progressive deformation. Relatively recent studies of magnetic anisotropy in the Barbados (Hounslow, 1990) and Nankai (Owens, 1993) accretionary prisms have provided evidence for the development of penetrative mineral fabrics in accreting sediments. These studies both suffered from either incomplete (Hounslow, 1990) or no (Owens, 1993) identification of the mineralogical sources of magnetic susceptibility in the specimens. Because all minerals contribute to the measured (low-field) magnetic susceptibility, variations in mineralogy can produce changes in the magnetic anisotropy fabrics that are greater than those produced by changes in mineral preferred orientation due to deformation. Additionally, to use magnetic anisotropy measurements as a proxy for finite strains in deformed sediments, the susceptibility carriers must be identified (Borradaile, 1991).

With these previous results in mind, we have conducted a study of magnetic anisotropy in conjunction with rock magnetic measurements designed to determine the major sources of magnetic susceptibility in sediments collected from the Cascadia accretionary prism during Ocean Drilling Program Leg 146. Five sites were drilled (Sites 888 through 892) in two areas, one off of Vancouver Island, the other off of the Oregon coast (Fig. 1). From these sites, a total of 495 specimens were measured for this study.

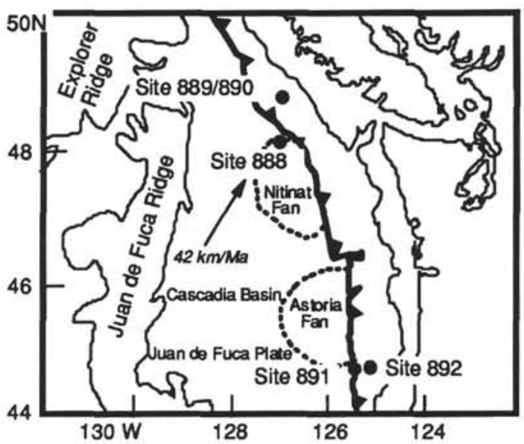

Figure 1. Location map of Sites 888, 889/890, 891, and 892 drilled during Ocean Drilling Program Leg 146.

METHODS

Anisotropy of magnetic susceptibility measurements were made using KLY-2 Kappabridge magnetic susceptibility devices at the University of Michigan Paleomagnetism Laboratory, and at the Hawaii Institute for Geophysics. The KLY-2 uses a low applied field (H = 0.08 mT at a frequency of 800 Hz) to generate an induced magnetization (J) in the specimen, the intensity of which is proportional to the low-field magnetic susceptibility (k = H/J). The specimens are measured in 15 orientations to define the susceptibility tensor (k_{ij}), from which the magnitudes and directions of the principal susceptibilities ($k_{max} \geq k_{int} \geq k_{min}$) are calculated.

To determine the mineralogical sources of the magnetic susceptibility, measurements of high-field (300 mT <H <1000 mT) magnetic

[1]Carson, B., Westbrook, G.K., Musgrave, R.J., and Suess, E. (Eds.), 1995. *Proc. ODP, Sci. Results*, 146 (Pt. 1): College Station, TX (Ocean Drilling Program).

[2]University of Michigan, Department of Geological Sciences, 1006 C.C. Little Science Building, Ann Arbor, Michigan, 48109-1063, U.S.A. (Present address: Institute for Rock Magnetism, University of Minnesota, 293 Shepherd Labs., 100 Union St. SE, Minneapolis, MN 55455-0128, U.S.A.)

[3]Faculty of Engineering, Niigata University, Ikarashi 2-nocho 8050, Niigata 950-21, Japan.

susceptibility were made on 121 of the specimens using a Princeton instruments Vibrating Sample Magnetometer (VSM) at the Institute for Rock Magnetism in the University of Minnesota. Above the saturation magnetization of the ferrimagnetic minerals (e.g., magnetite, greigite, pyrrhotite) in the sediments, the increase in magnetization produced by increasing the applied field is proportional to the sum of the paramagnetic, antiferromagnetic, and diamagnetic susceptibilities of the specimen (Fig. 2). In these clay-rich specimens no antiferromagnetic minerals were found, and the diamagnetic contribution (quartz, silica, and carbonates) will be negligible compared to that of the paramagnetic clays (Borradaile et al., 1987). By comparing the high-field susceptibilities with the low-field susceptibilities, the relative contributions of the paramagnetic clays and ferrimagnetic trace minerals can be determined.

Additional characterization of the ferrimagnetic trace minerals was made by thermal demagnetization of multi-component Isothermal Remanent Magnetization (mIRM) (Lowrie, 1990). For this method IRM components (low coercivity [0.05 or 0.1 T], medium coercivity [0.4 T], and high coercivity [1.3 or 1.4 T]) were given to specimens in orthogonal directions using an electromagnet. The specimens were then thermally demagnetized in 15 to 20 steps from room temperature to 650°C, with the remanence measured after each thermal step. By comparing the thermal-unblocking temperature with the applied field of the mIRM components, the magnetic minerals in a specimen can be identified (see Lowrie, 1990 for further details). These measurements were made using the magnetometers at the University of Michigan Paleomagnetism Laboratory and the Kyoto University Paleomagnetic Laboratory.

Another magnetic anisotropy method, Anhysteretic Remanent Magnetization Anisotropy (ARMA) (McCabe et al., 1985) was used to determine the preferred orientation of the ferrimagnetic minerals. This method was used to constrain the ferrimagnetic fabrics in two of the sites where the low-field susceptibility was carried by both paramagnetic and ferrimagnetic minerals. Using a DC coil to generate a 0.1 mT biasing field, an ARM is imparted to the specimen using an alternating field demagnetizer. The ARMA tensor is calculated from the results of ARMs given in nine separate orientations, according to the scheme of Girdler (1961). The Sapphire Instruments SI-4 a.f. demagnetizer in the University of Michigan Paleomagnetism Laboratory is equipped to further refine the ARMA method by allowing a partial ARM (pARM) to be imparted to a specimen over a narrow alternating field window. Using the method of Jackson et al., 1988, pARMs are given to each specimen over a 10 mT wide window, in increments from 0 to 160 mT. The magnetization of the specimen was measured with a 2-G cryogenic magnetometer after each pARM step. The distribution of pARM intensities over this range is used to determine the optimum range over which to generate the ARM for the ARMA experiments.

From each core (9.5 meters of sediment), one to five specimens were collected in one of three ways: as 6 cm^3 cubes carved out of the sediment with a scalpel, as 12 cm^3 octagonal cylinders carved or pressed into the sediment, or as 12 cm^3, 2.5 cm diameter, 2.2 cm long paleomagnetic "minicores" drilled from epoxy-encapsulated sediments. The epoxy-encapsulated specimens were prepared by immersing a 20- to 40-cm^3 quarter-round specimen in a paper cup filled with epoxy mixed with ether (to lower the viscosity of the epoxy). The specimen was placed in a vacuum chamber for 10 to 25 minutes to remove air trapped in fractures. The sample chamber was then pressurized to 800 to 1000 psi with nitrogen gas for eight to ten hours. This process fills the fractures (and a limited amount of pore space) with epoxy, allowing the minicores to be drilled from these unconsolidated sediments. Please note that the declinations of the AMS orientations at all of the sites in this study are in arbitrary "core" coordinates (i.e., have no horizontal orientation), as all specimens are not corrected for rotation of the specimens as they were drilled. Attempts were made to reorient the cores using paleomagnetism, but because of the low quality of the paleomagnetic data for the majority of the specimens, reorientation of the cores into true geographic coordinates can not be made with confidence.

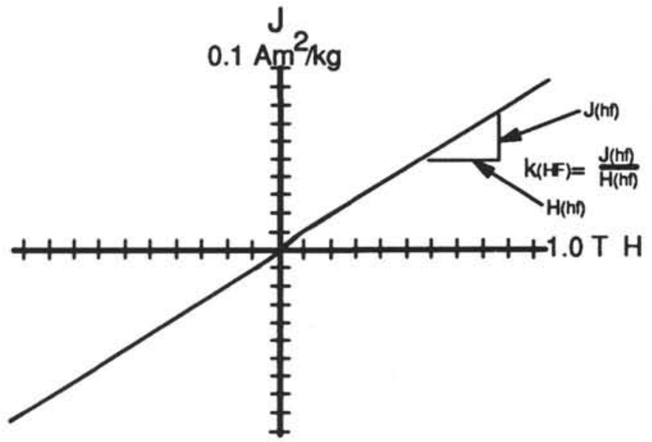

Figure 2. Hysteresis loop used to determine high-field (paramagnetic) susceptibility in samples from Leg 146. The vertical axis is measured magnetization in the sample (J, Am^2/kg), and the horizontal axis is applied magnetic field (H, T). The ferrimagnetic minerals in these samples reach saturation magnetization between 0.1 T and 0.4 T. Above this value, the linear increase of J with increasing H is proportional to the paramagnetic susceptibility (k_{para}), assuming negligible contributions from antiferromagnetic phases and diamagnetic carbonates and silica.

RESULTS

Site 888

Site 888 is on the edge of the Nitinat Fan off of Vancouver Island (Fig. 1) and was drilled as an undeformed reference site. The drilled interval (0 to 567 meters below sea floor [mbsf]) is composed of a succession of turbidites. Three lithologic units were defined during shipboard work: Unit I (0–193 mbsf), composed of clayey silt with interbedded sand, Unit II (193–452.1 mbsf), composed of very fine to medium siliciclastic sand with intervals of coarse sand and clayey silt, and Unit III (452.1–567 mbsf), composed of clayey silt with sand and pebbles (Westbrook, Carson, Musgrave, et al., 1994).

Comparison of high-field and low-field susceptibility values of Site 888 specimens indicates that paramagnetic minerals contribute less than 7% of the low-field susceptibility and that there is little downhole variability in the relative contributions of the ferrimagnetic and paramagnetic minerals to susceptibility (Fig. 3). The AMS results from this site will thus provide preferred orientations of the ferrimagnetic minerals in these sediments. The mIRM results from this site are all dominated by the low coercivity (0.1 T) component. This component has two thermal unblocking temperatures (T_{ub}): one at about 310°C, the other between 550° and 590°C (Fig. 4). The low-coercivity, low-T_{ub} component is carried by either pyrrhotite or greigite (maghemite is ruled out by the reducing conditions of pore waters at Site 888 (Westbrook, Carson, Musgrave, et al., 1994)), and the low-coercivity, high-T_{ub} component is carried by magnetite (Lowrie, 1990). Both the magnetic sulfides and magnetite are present throughout Site 888, so the AMS results will be a composite fabric representing magnetite dimensional preferred orientations and greigite/pyrrhotite crystallographic preferred orientations. Because magnetite has a much higher susceptibility than either of the magnetic sulfides (Borradaile et al., 1987), the AMS fabrics most likely are controlled by the magnetite orientations.

The AMS results from Site 888 (Table 1) are consistent with the structures observed at this undeformed reference site. The orientations of the minimum susceptibility axes are sub-vertical throughout

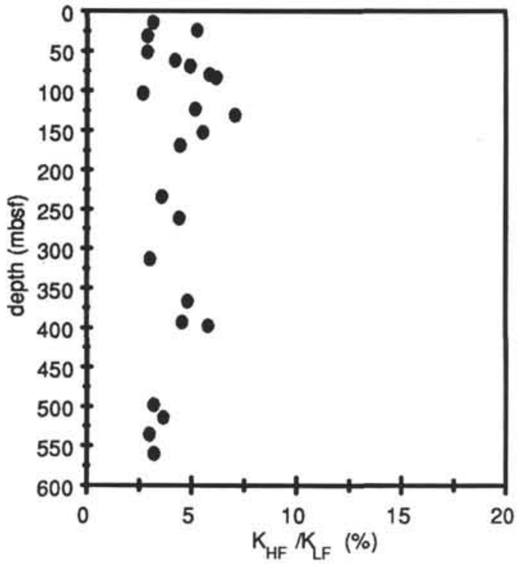

Figure 3. Depth (mbsf) vs. the percentage of low-field magnetic susceptibility carried by the paramagnetic minerals in sediments from Site 888, as determined by comparing the high-field and low-field susceptibilities. Here, the majority (>90%) of the low-field susceptibility is carried by the ferrimagnetic minerals.

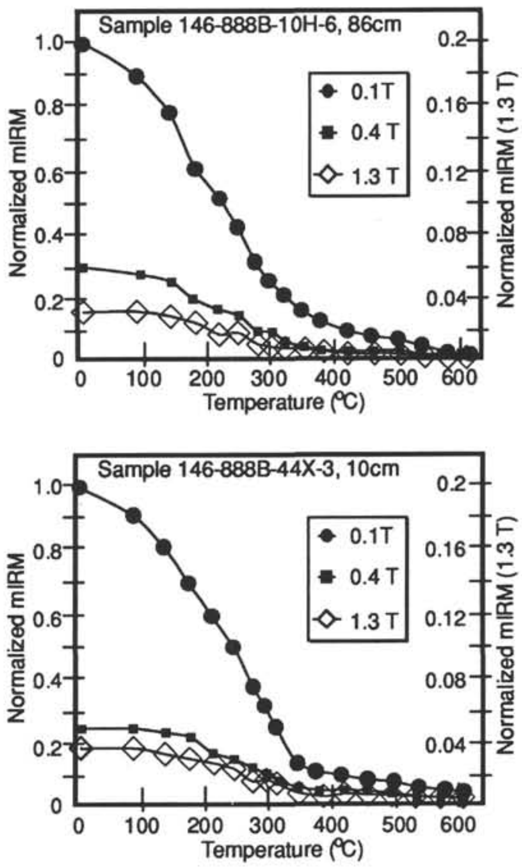

Figure 4. Thermal demagnetization of multi-component Isothermal Remanent Magnetization (mIRM) results from two representative samples from Site 888. The left vertical axis is normalized magnetization of the 0.1 T and 0.4 T mIRM components, the right vertical axis is the normalized intensity of the 1.4 T mIRM component. The horizontal axis is the temperature of the thermal demagnetization step (°C). In all Site 888 samples the 0.1 T component carries most of the mIRM, and two thermal unblocking temperatures (T_{ub}), (one at about 300°C, the other at about 580°C) are observed. This indicates that both greigite and/or pyrrhotite (T_{ub} ~300°C) and magnetite (T_{ub} ~580°C) are the dominant magnetic minerals in these sediments.

the hole (Fig. 5A–C), agreeing with the shipboard observations of sub-horizontal bedding at this site (Westbrook, Carson, Musgrave, et al., 1994). The shapes of the susceptibility ellipsoids are predominantly oblate, with variable degrees of anisotropy (Fig. 5D–F). There is no noticeable trend relating either the degree of anisotropy ($P = k_{max}/k_{min}$) or of the degree of oblateness ($F = k_{int}/k_{min}$) with depth in specimens from Units I and II. An increase in degree of anisotropy with depth is found in Unit III specimens (Table 1), which is consistent with observations of decreasing porosity with depth in Unit III (Westbrook, Carson, Musgrave, et al., 1994).

Site 889/890

Sites 889 and 890 were drilled in the Cascadia accretionary prism to the north of Site 888 (Fig. 1). The sediments are primarily clayey silts and silty clays, and were divided into three structural domains based on shipboard observations. Structural domain I (0–104 mbsf) consists of slope sediments with sub-horizontal bedding. Structural domain II (104–127 mbsf) is marked by beds that dip from 36° to 74° and may represent either a sedimentary slump or a tectonically tilted block. Structural domain III (127 to 380 mbsf) is characterized by the progressive development of a weak fracture fabric (with dips from 40° to 60°), incipient scaly foliation, and occasional deformation bands (Westbrook, Carson, Musgrave, et al., 1994).

Comparison of the high-field and low-field susceptibilities for Site 889/890 specimens indicates a complex variation in the susceptibility carriers in these sediments. The percentage of the low-field susceptibility carried by paramagnetic minerals (k_{HF}/k_{LF}) varies from less than 5% to 80% (Fig. 6). There is no clear relationship (with the exception of the uppermost 40 meters of sediment) between either lithological variations, structural variations, and the variation in susceptibility carriers. The values of paramagnetic susceptibility (high-field susceptibility) are relatively constant downhole, so the large variations in k_{HF}/k_{LF} can be attributed to variations in the amount and species (or both) of the ferrimagnetic minerals. The mIRM results (Fig. 7) reflect this variation. Most of the specimens are dominated by the low coercivity (0.05 T) component, but several specimens also have significant contributions from the 0.4 and 1.4 T components as well. These higher coercivity components indicate that fine-grained magnetite and/or pyrrhotite are present in the Site 889/890 specimens. Like the Site 888 specimens, two unblocking temperatures (one at about 310°C, the other between 550° and 590°C) are observed, indicating the presence of both magnetic sulfides and magnetite. (Again, the reducing conditions at this site rule out maghemite for the low T_{ub} component. In a few of the specimens the mIRM is carried almost entirely by the 310°C T_{ub} component (Fig. 7C). The AMS measurements from Site 889/890 specimens will thus represent composite fabrics of paramagnetic clays, magnetite, and magnetic sulfides.

Because the AMS results will record the sum of these depositional, deformation, and diagenetic fabrics, the use of AMS as an indicator of structure must account for the occurrence of composite magnetic fabrics. Experiments and numerical models on composite magnetic fabrics have shown that the shape of the susceptibility ellipsoid is most sensitive to the effects of composite fabrics, while the orientation of the minimum AMS axis is relatively insensitive to

Table 1. Anisotropy of magnetic susceptibility (AMS) data for Site 888.

Core, section, interval (cm)	Depth (mbsf)	K_{max} Dec	K_{max} Inc	K_{int} Dec	K_{int} Inc	K_{min} Dec	K_{min} Inc	K_{max} (1×10^{-6})	K_{int} (1×10^{-6})	K_{min} (1×10^{-6})	K_{mean} (1×10^{-6})	L	F	P	AMS dip
146-888B-															
1H-3, 42	3.4	210	18	302	7	51	71	956.4	944.0	932.7	944.4	1.01	1.01	1.03	19
1H-6, 38	7.9	240	58	61	32	330	0	2372.5	2276.4	2188.6	2279.2	1.04	1.04	1.08	90
2H-2, 54	11.5	89	34	209	36	330	36	2726.8	2690.0	2604.2	2673.7	1.01	1.03	1.05	54
2H-7, 9	14.6	212	16	121	2	23	74	2475.4	2446.6	2161.5	2361.2	1.01	1.13	1.15	16
3H-2, 45	17.0	173	2	263	3	44	86	1753.4	1745.9	1488.8	1662.7	1.00	1.17	1.18	4
3H-7, 54	24.5	277	3	186	16	15	74	2129.9	2101.7	1896.2	2042.6	1.01	1.11	1.12	16
4H-3, 56	28.1	223	7	133	6	2	81	2204.5	2180.0	1885.7	2090.1	1.01	1.16	1.17	9
4H-5, 88	31.4	246	5	336	0	67	85	3902.9	3861.4	3446.2	3736.8	1.01	1.12	1.13	5
5H-4, 65	39.2	260	7	170	0	77	83	2915.8	2906.8	2477.8	2766.8	1.00	1.17	1.18	7
5H-6, 45	42.0	118	52	228	15	328	34	3209.3	3096.5	3072.8	3126.2	1.04	1.01	1.04	56
6H-2, 72	45.7	176	8	266	1	2	82	2721.8	2712.2	2233.9	2556.0	1.00	1.21	1.22	8
6H-6, 67	51.7	210	12	120	1	26	78	2488.9	2425.0	2122.8	2345.6	1.03	1.14	1.17	12
7H-4, 88	58.4	219	10	310	3	57	79	2070.0	2056.2	1911.6	2012.6	1.01	1.08	1.08	11
7H-7, 44	62.5	174	3	265	6	60	84	2976.7	2954.1	2501.6	2810.8	1.01	1.18	1.19	6
8H-5, 92	69.4	190	5	99	3	335	84	2060.6	2024.1	1833.6	1972.8	1.02	1.10	1.12	6
8H-6, 26	70.3	185	13	95	2	354	77	2667.8	2585.3	2271.7	2508.3	1.03	1.14	1.17	13
9H-2, 67	74.2	194	8	286	10	66	77	2747.9	2694.6	2529.4	2657.3	1.02	1.07	1.09	13
9H-6, 64	80.2	3	13	273	0	182	77	2062.8	2037.5	1899.8	2000.0	1.01	1.07	1.09	13
10H-2, 79	83.8	188	11	98	0	7	79	2084.6	2044.0	1728.9	1952.5	1.02	1.18	1.21	11
10H-6, 86	89.9	290	7	199	9	59	79	3884.3	3682.4	3237.4	3601.4	1.05	1.14	1.20	11
11H-2, 30	92.8	204	5	294	2	48	84	2016.6	1991.4	1839.9	1949.3	1.01	1.08	1.10	6
11H-5, 40	97.3	199	12	289	4	39	77	2776.4	2728.5	2625.5	2710.1	1.02	1.04	1.06	13
11H-6, 115	99.5	190	60	335	25	72	15	3475.4	3374.3	3267.0	3372.2	1.03	1.03	1.06	75
12H-1, 17	100.7	162	27	64	14	310	59	6699.5	6149.6	5583.9	6144.3	1.09	1.10	1.20	31
12H-3, 10	103.6	194	34	76	35	315	37	6718.9	6313.9	6258.7	6430.5	1.06	1.01	1.07	53
13H-1, 13	108.7	147	18	53	12	292	68	1792.2	1757.8	1663.0	1737.7	1.02	1.06	1.08	22
13H-2, 38	110.5	175	60	325	27	62	13	2051.0	2024.6	2000.9	2025.5	1.01	1.01	1.03	77
13H-4, 72	113.8	144	14	53	2	314	76	2716.9	2663.4	2603.7	2661.3	1.02	1.02	1.04	14
14H-1, 89	119.0	209	11	302	15	84	71	2249.1	2122.0	1940.4	2103.8	1.06	1.09	1.16	19
14H-2, 40	120.0	260	30	15	37	142	39	2604.6	2565.2	2236.4	2468.8	1.02	1.15	1.16	51
14H-3, 133	122.4	229	13	136	14	2	71	2359.9	2305.6	2108.8	2258.1	1.02	1.09	1.12	19
14H-4, 110	123.7	168	3	78	5	288	84	2531.1	2423.0	2189.3	2381.1	1.04	1.11	1.16	6
15H-1, 136	129.0	175	37	267	2	360	52	1465.4	1313.6	1021.3	1266.8	1.12	1.29	1.43	38
15H-2, 80	129.9	210	8	119	2	18	82	1241.4	1219.3	1069.8	1176.8	1.02	1.14	1.16	8
15H-3, 60	131.2	203	15	294	2	32	75	1231.6	1219.4	1067.9	1173.0	1.01	1.14	1.15	15
15H-4, 10	132.2	204	2	114	1	7	88	1480.0	1448.3	1321.0	1416.4	1.02	1.10	1.12	2
16H-1, 80	137.9	237	8	145	15	354	73	1925.9	1866.0	1672.9	1821.6	1.03	1.12	1.15	17
16H-3, 57	140.7	209	15	119	1	27	75	2076.2	2045.7	1829.1	1983.7	1.01	1.12	1.14	15
17H-3, 82	150.4	195	17	105	1	13	73	2360.0	2229.9	1962.9	2184.3	1.06	1.14	1.20	17
17H-5, 45	153.1	212	29	302	1	33	61	2304.9	2217.2	2071.5	2197.9	1.04	1.07	1.11	29
19X-3, 59	169.2	203	9	294	4	47	80	2292.3	2281.9	1997.7	2190.6	1.00	1.14	1.15	10
19X-4, 97	171.1	2	1	92	5	257	85	2205.6	2194.6	1953.3	2117.8	1.01	1.12	1.13	5
27H-1, 27	234.5	103	26	195	5	295	63	2007.2	1820.6	1654.9	1827.6	1.10	1.10	1.21	27
28H-1, 53	243.8	177	22	268	4	7	68	2486.8	2419.5	2192.4	2366.2	1.03	1.10	1.13	22
30H-1, 118	262.0	160	24	264	29	37	51	2092.4	2068.0	2015.8	2058.7	1.01	1.03	1.04	39
33H-1, 40	283.2	195	36	100	6	2	53	5070.0	5029.8	4882.9	4994.2	1.01	1.03	1.04	37
36H-1, 36	310.4	210	1	120	4	309	86	2595.4	2556.9	2390.6	2514.3	1.02	1.07	1.09	4
36H-4, 60	313.3	155	18	245	1	340	72	1877.1	1848.5	1798.4	1841.3	1.02	1.03	1.04	18
42X-1, 22	366.7	273	0	3	1	161	89	2144.7	2076.3	1769.6	1996.9	1.03	1.17	1.21	1
42X-2, 107	367.3	125	29	216	1	307	61	2775.4	2669.2	2427.0	2623.9	1.04	1.10	1.14	29
44X-6, 2	393.0	215	13	124	3	22	77	1838.6	1818.0	1608.6	1755.1	1.01	1.13	1.14	13
45X-1, 18	395.2	188	1	279	2	69	88	1927.3	1902.2	1791.9	1873.8	1.01	1.06	1.08	2
45X-2, 113	397.6	70	3	160	1	269	87	2261.5	2243.2	2044.2	2183.0	1.01	1.10	1.11	3
57X-2, 101	498.7	281	24	189	5	87	66	3820.4	3812.2	3324.1	3652.2	1.00	1.15	1.15	24
57X-3, 107	500.3	61	4	330	15	165	74	4757.9	4718.3	4454.9	4643.7	1.01	1.06	1.07	16
59P-1, 43	514.4	48	6	138	4	257	83	3135.4	3009.9	2722.9	2956.1	1.04	1.11	1.15	7
60X-CC, 21	515.6	240	1	330	11	144	79	2600.6	2580.6	2230.0	2470.4	1.01	1.16	1.17	11
61X-1, 145	524.3	173	7	265	16	61	72	4197.2	3974.5	3701.4	3957.7	1.06	1.07	1.13	18
62X-3, 119	535.7	183	16	90	9	333	71	4383.2	4105.6	3475.6	3988.2	1.07	1.18	1.26	19
62X-CC, 12	535.9	110	11	20	4	269	79	4685.4	4672.5	3817.6	4391.8	1.00	1.22	1.23	11
64X-1, 71	549.9	27	4	297	11	135	78	4248.3	4032.7	3420.5	3900.5	1.05	1.18	1.24	12
65X-2, 68	560.3	201	24	108	7	3	65	4447.4	3906.6	3547.3	3967.1	1.14	1.10	1.25	25

Notes: Dec = declination (degrees); Inc = inclination (degrees); K_{max}, K_{int}, K_{min}, K_{mean} in SI volume units; $L = K_{max}/K_{int}$; $F = K_{int}/K_{min}$; $P = K_{max}/K_{min}$; AMS dip = (90 – K_{min} inc).

composite fabrics (Housen et al., 1993). In most cases the minimum AMS axis reflects the orientation of the dominant planar fabric (i.e., bedding or cleavage) in a specimen. The minimum AMS axes will thus serve as an accurate measure of the orientations of the dominant planar fabrics in the sediments from this site. Because composite fabrics tend (when the component fabrics are not parallel to each other) to depress the degree of anisotropy, the results from this site should be viewed as minimum estimates of the anisotropy of the dominant fabric.

The AMS results from Site 889/890 (Table 2) agree well with the observed structures, given the complexities of the susceptibility carriers at this site. In structural domain I the AMS foliations (the plane perpendicular to the minimum axis) are predominantly sub-horizontal, reflecting the shallowly dipping bedding recorded in the upper 104 m of the sediment (Fig. 8A and B). The shapes of the susceptibility ellipsoids vary from moderately prolate to highly oblate (Fig. 8E and F). In structural domain II the AMS foliations are either steeply dipping (52° to 85°) or sub-horizontal (Fig. 8C). The steep magnetic foliations accurately reflect the moderately to steeply dipping bedding that characterizes structural domain II. The shapes of the susceptibility ellipsoids in these specimens are very weakly anisotropic and scattered (Fig. 8G). The AMS fabrics from structural domain III are highly variable in orientation (Fig. 8D), with weakly anisotropic susceptibility ellipsoids (Fig. 8H). Closer examination of the data reveals that the shallowly dipping AMS fabrics occur where shallowly dipping bedding was measured during shipboard observation of

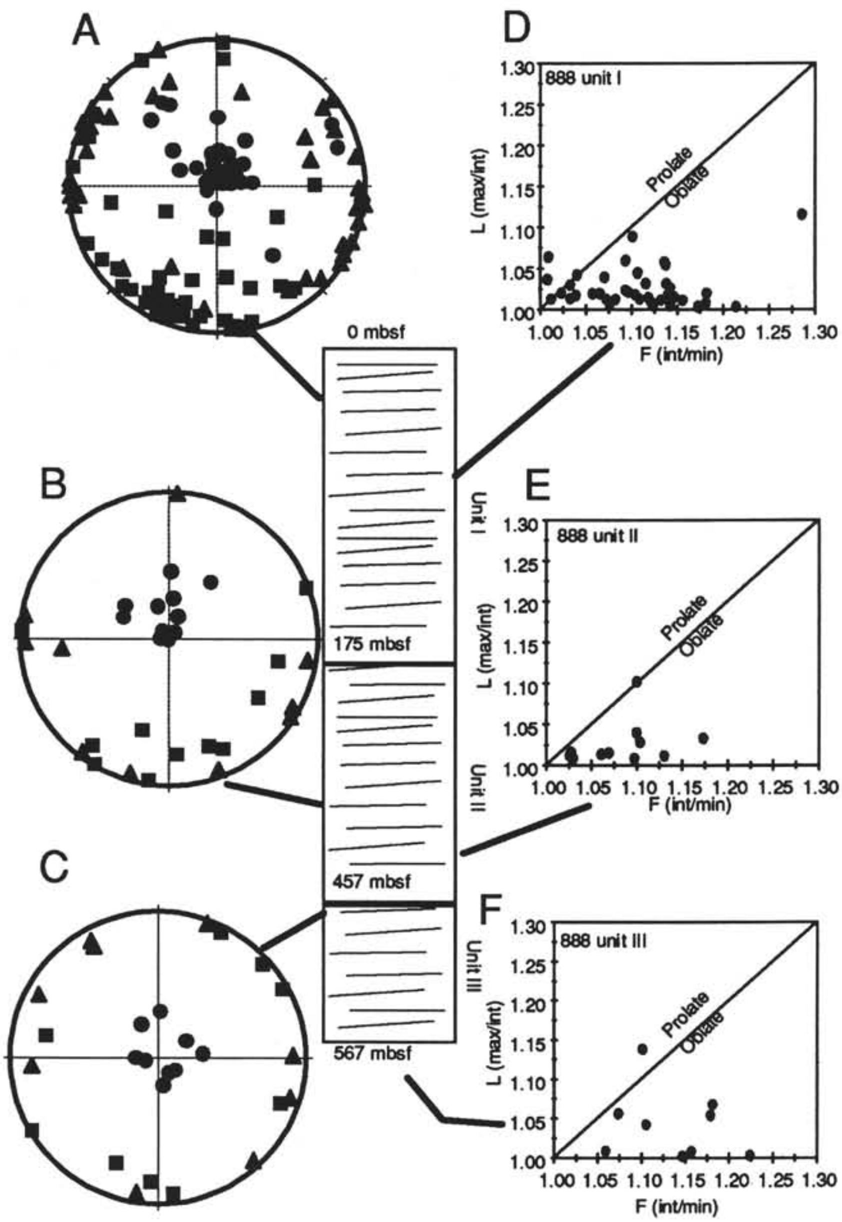

Figure 5. Anisotropy of magnetic susceptibility results from Site 888. The basic structures (subhorizontal bedding) and lithologic unit boundaries are denoted in the schematic column. **A–C.** Equal-area stereographic projections of the principal susceptibility axes (k_{max} = solid squares, k_{int} = solid triangles, k_{min} =solid circles) orientations for each lithologic unit. Note that the declinations of the axes are in un-oriented core coordinates. The minimum axes for almost all samples are steeply dipping. **D–F.** The shapes of the susceptibility ellipsoids are shown on Flinn-type diagrams. Vertical axes are magnetic lineation ($L = k_{max}/k_{int}$) and horizontal axes are magnetic foliations ($F = k_{int}/k_{min}$). For almost all samples, the AMS ellipsoids are nearly uniaxial-oblate in shape.

the cores. Where steeply dipping AMS fabrics occur, fractures with dips between 40° and 60° are the dominant structures (Westbrook, Carson, Musgrave, et al., 1994). The close agreement between the fracture dips and the AMS fabric dips suggests that the AMS fabrics reflect the dominant fracture orientation. Within one such location (Sample 146-889A-41X-2, 103 cm) steeply dipping bedding was also measured, so the fracture orientations (and AMS) could represent bedding in these sub-domains as well.

Measurement of the preferred orientation of the ferrimagnetic minerals, using ARMA, avoids the effects of composite fabrics that arise from variations in the low-field susceptibility carriers. Because both magnetite and magnetic sulfides are present, however, composite ARMA fabrics may still occur in these specimens. The coercivity spectra of specimens from Site 889 are similar throughout the section, with a peak in the pARM curves between 15 and 35 mT (Fig. 9). An alternating field window from 5 to 60 mT was selected for the ARMA experiments. The ARMA results (Table 3) agree fairly well with the AMS fabrics. In structural domain I the ARMA foliation dips from 4° to 59° (Fig. 10A). All of the ARMA dips greater than 30° occur between 79 and 90 mbsf, and may represent a slump block within this interval. The lack of ARMA fabrics with dips greater than 60° in this interval (in contrast to the steep dips of the AMS foliations in several specimens) indicates that the steep AMS foliation dips are most likely inverse magnetic fabrics (Rochette, 1987; Potter and Stephenson, 1988) arising from elongate single-domain magnetites. The shapes of the ARMA ellipsoids vary between prolate to strongly oblate (Fig. 10D). In structural domain II ARMA dips are all between 60° and 90°, which agrees very well with the bedding dips in this domain (Fig. 10B). The shapes of the ARMA ellipsoids are nearly triaxial (Fig. 10E). The ARMA foliations in structural domain III have more widely variable dips, ranging from 7° to 75° (Fig. 10C). In most cases ARMA and AMS foliations from the same interval have similar dips. The shapes of the ARMA ellipsoids in domain III vary from weakly prolate to strongly oblate (Fig. 10F).

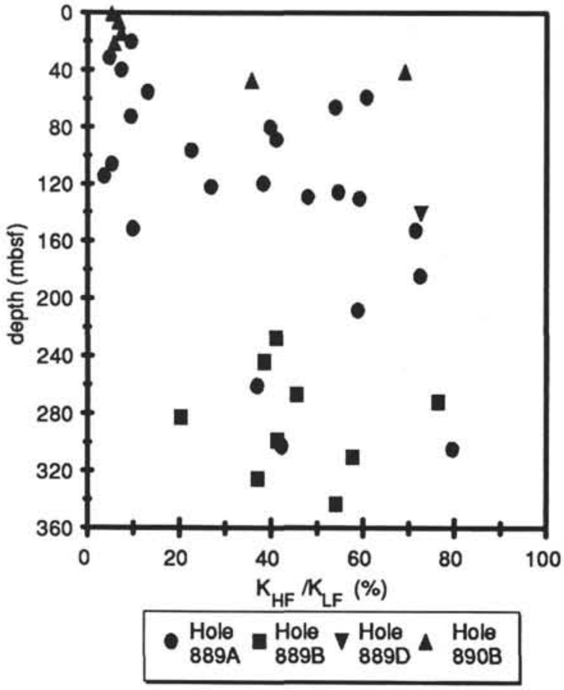

Figure 6. Depth (mbsf) vs. the percentage of low-field magnetic susceptibility carried by the paramagnetic minerals in sediments from Site 889/890, as determined by comparing the high-field and low-field susceptibilities. The low-field susceptibility carriers vary between greater than 90% ferrimagnetic minerals in the upper 40 meters, to 80% paramagnetic minerals deeper in the section.

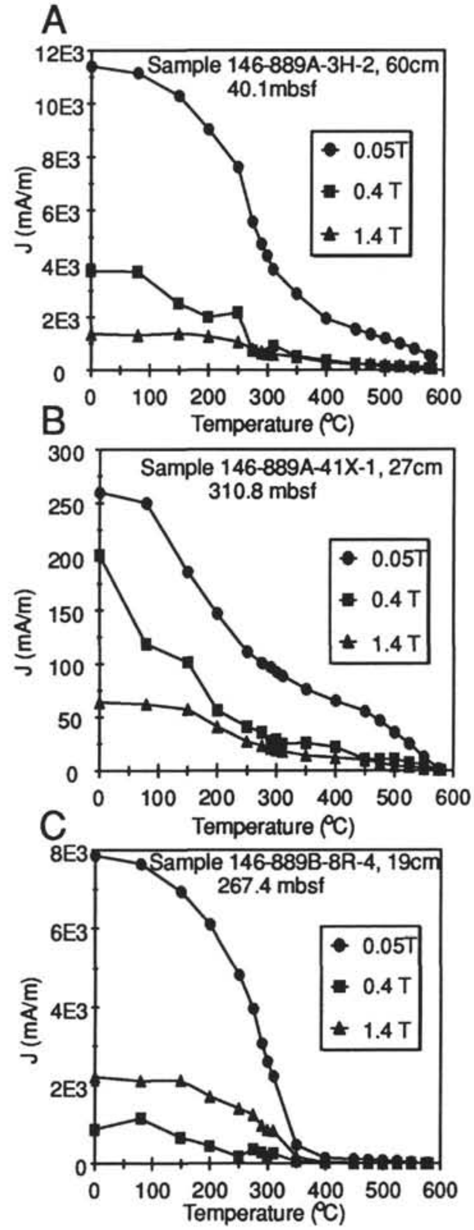

Figure 7. Thermal demagnetization of mIRM results for representative Site 889/890 samples. The vertical axes are magnetization of the mIRM components (mA/m), the horizontal axes are temperature of the thermal demagnetization step. **A.** Sample dominated by the 0.05 T component, with two thermal unblocking temperatures (T_{ub}), one at about 300°C, the other at about 580°C. This indicates that both greigite and/or pyrrhotite (T_{ub} ~300° C) and magnetite (T_{ub} ~580° C) are the dominant magnetic minerals in this sample. **B.** Sample with strong contributions from both the 0.05 T and 0.4 T components, with T_{ub} similar to those in A. **C.** Sample dominated by 0.05 T (with a relatively strong 1.4 T component), which is carried almost entirely by greigite or pyrrhotite, indicated by the removal of nearly all the mIRM after the 320°C step.

Site 891

Site 891 was drilled across the frontal thrust in the Cascadia accretionary prism off of the Oregon coast (Fig. 1). Core recovery at this site was about 10% (and in the upper 100 meters less than 2%), which hampered interpretation of the section. The lithology of the drilled interval was fairly uniform, consisting of clayey silt, silt, and fine to medium sand intervals. Based on the limited information, five structural domains were defined during shipboard observations (Westbrook, Carson, Musgrave, et al., 1994). Structural domain I (0–198 mbsf) is characterized by steeply dipping bedding with occasional deformation bands. Structural domain II (198–95 mbsf) is marked by fracture fabrics of various intensity, which dip between 30° and 60°. Structural domain III (295–321 mbsf) is defined by a bedding-parallel fissility, without any noticeable fracture fabric. Structural domain IV (321–383 mbsf) has a well-developed, steeply dipping fracture fabric. Structural domain V (383–472 mbsf) is characterized by weak, bedding-parallel fissility and a lack of fracture fabrics.

Comparison between the high-field and low-field susceptibilities (Fig. 11) indicates that for most of the section less than 10% of the low-field susceptibility is carried by paramagnetic minerals, so the AMS results will reflect the fabrics of the ferrimagnetic minerals. The mIRM results (Fig. 12) show that the low-coercivity (0.1 T) component carries the majority of the mIRM. This component has two thermal unblocking temperatures (one at about 310°C, the other between 550° and 590°C). The unblocking temperatures, combined with the reducing conditions in the pore waters (Westbrook, Carson, Musgrave, et al., 1994), indicates that both magnetic sulfides (greigite and/or pyrrhotite) and magnetite are the most abundant ferrimagnetic minerals in these sediments, and so the AMS fabrics will be controlled by the orientations of these minerals.

The AMS results from Site 891 (Table 4) agree well with the observed structural fabrics. In structural domain I (Fig. 13A), the AMS foliations dip between 50° and 88°, which agrees closely with the measured bedding dips in this interval. The shapes of the AMS ellipsoids are predominantly oblate (Fig. 13F) and moderately to highly anisotropic. The specimens with prolate AMS ellipsoids occur near deformation bands in Cores 146-891B-20X to 23X. In structural domain II the AMS fabrics are much more variable in orientation (Fig.

Table 2. Anisotropy of magnetic susceptibility (AMS) data for Site 889/890.

Core, section, interval (cm)	Depth (mbsf)	K_{max}		K_{int}		K_{min}		K_{max} (1×10^{-6})	K_{int} (1×10^{-6})	K_{min} (1×10^{-6})	K_{mean} (1×10^{-6})	L	F	P	AMS dip
		Dec	Inc	Dec	Inc	Dec	Inc								
146-889A-															
1H-1, 29	20.3	247	9	155	10	20	77	1093.8	1031.3	1003.9	1043.0	1.06	1.03	1.09	13
2H-2, 66	31.7	99	7	188	1	2	89	1177.6	1164.5	1116.8	1153.0	1.01	1.04	1.05	1
2H-6, 109	38.1	152	13	243	5	353	76	887.8	878.4	858.7	875.0	1.01	1.02	1.03	14
3H-2, 60	40.1	94	3	184	9	344	80	768.9	758.6	728.4	752.0	1.01	1.04	1.06	10
3H-5, 36	44.4	140	12	232	9	357	75	501.2	491.5	468.3	487.0	1.02	1.05	1.07	16
3H-7, 82	47.9	145	12	237	7	355	76	848.9	839.1	820.0	836.0	1.01	1.02	1.04	14
4H-5, 74	54.0	329	1	238	25	62	65	1718.6	1690.7	1654.5	1687.9	1.02	1.02	1.04	26
4H-6, 78	55.5	163	8	254	7	28	80	319.3	314.0	308.7	314.0	1.02	1.02	1.03	11
4H-CC, 30	58.4	244	16	347	38	135	47	232.5	221.2	218.3	224.0	1.05	1.01	1.07	43
5H-1, 102	59.0	208	13	115	16	336	70	129.5	129.3	128.2	129.0	1.00	1.01	1.01	21
5H-2, 14	59.6	8	68	149	18	243	13	115.5	115.2	114.3	115.0	1.00	1.01	1.01	77
5H-6, 69	66.2	179	3	270	16	78	74	106.6	105.2	103.2	105.0	1.01	1.02	1.03	17
6H-1, 22	67.7	169	11	261	12	39	74	130.5	124.3	123.2	126.0	1.05	1.01	1.06	16
6H-2, 96	69.1	341	21	74	5	176	68	244.8	235.0	228.2	236.0	1.04	1.03	1.07	22
6H-3, 121	70.8	140	2	230	2	10	87	1251.1	1210.4	1117.4	1193.0	1.03	1.08	1.12	3
6H-3, 121	70.8	151	9	60	6	295	79	1707.0	1659.2	1475.7	1614.0	1.03	1.12	1.16	11
6H-4, 115	72.0	149	11	56	17	270	69	1234.6	1166.2	1160.1	1187.0	1.06	1.01	1.06	21
6H-5, 46	72.7	333	30	196	52	77	21	674.3	655.9	646.8	659.0	1.03	1.01	1.04	69
7H-1, 89	77.9	303	21	170	60	41	20	106.7	106.5	104.9	106.0	1.00	1.02	1.02	70
7H-3, 7	80.1	297	8	39	56	202	33	114.2	113.1	111.7	113.0	1.01	1.01	1.02	57
8H-1, 40	86.9	202	20	107	12	348	66	146.6	145.0	137.4	143.0	1.01	1.06	1.07	24
8H-2, 39	88.4	240	11	143	31	347	57	140.6	138.4	135.0	138.0	1.02	1.03	1.04	34
8H-4, 29	91.3	222	11	125	34	327	54	100.8	99.9	96.3	99.0	1.01	1.04	1.05	36
9H-2, 33	96.3	262	14	1	30	151	56	103.7	103.2	102.1	103.0	1.01	1.01	1.02	34
9H-6, 82	101.5	73	22	327	34	189	48	925.0	904.2	894.7	908.0	1.02	1.01	1.03	43
10H-2, 60	106.1	306	80	150	10	60	4	1677.4	1599.6	1576.9	1618.0	1.05	1.01	1.06	86
11H-1, 93	114.4	298	10	207	2	107	80	1631.0	1530.7	1455.1	1538.9	1.07	1.05	1.12	10
12H-1, 62	119.6	142	10	38	56	238	33	109.5	109.0	108.5	109.0	1.00	1.00	1.01	58
12H-3, 72	122.1	243	56	351	12	89	32	170.5	170.4	169.1	170.0	1.00	1.01	1.01	58
12H-4, 67	123.3	310	53	48	6	142	36	93.4	93.4	92.2	93.0	1.00	1.01	1.01	54
12H-6, 22	125.8	226	80	88	8	356	7	94.2	92.6	92.2	93.0	1.02	1.00	1.02	83
14H-2, 32	128.9	125	8	216	5	338	80	60.3	60.2	59.6	60.0	1.00	1.01	1.01	10
17X-1, 12	130.2	95	10	185	5	300	79	76.9	76.0	75.1	76.0	1.01	1.01	1.02	11
17X-2, 14	130.9	222	8	129	18	334	70	61.4	61.2	60.4	61.0	1.00	1.01	1.02	20
18X-5, 72	145.2	316	5	226	2	112	84	75.4	74.7	71.9	74.0	1.01	1.04	1.05	6
19X-2, 75	151.4	336	67	191	20	97	12	479.7	457.4	454.9	464.0	1.05	1.01	1.05	78
19X-3, 75	152.7	133	13	38	23	250	63	56.6	56.3	55.1	56.0	1.00	1.02	1.03	27
20X-1, 69	159.3	286	6	189	51	21	38	84.3	82.9	81.8	83.0	1.02	1.01	1.03	52
20X-4, 118	164.0	160	71	66	2	335	19	108.2	107.6	105.2	107.0	1.01	1.02	1.03	71
22X-6, 111	184.6	260	0	350	4	167	86	75.9	75.3	73.9	75.0	1.01	1.02	1.03	4
26X-1, 142	208.2	284	31	17	5	115	58	97.0	96.5	94.5	96.0	1.00	1.02	1.03	32
34X-3, 82	261.0	91	14	0	4	253	75	124.1	123.0	118.9	122.0	1.01	1.03	1.04	15
40X-1, 137	302.9	116	1	26	23	207	67	114.5	113.3	111.2	113.0	1.01	1.02	1.03	23
40X-2, 137	304.4	55	0	145	54	325	36	98.8	96.9	95.3	97.0	1.02	1.02	1.04	54
40X-3, 27	304.8	2	0	271	57	92	33	94.3	93.5	91.2	93.0	1.01	1.02	1.03	57
40X-4, 129	307.3	176	2	84	47	268	43	103.2	102.5	100.3	102.0	1.01	1.02	1.03	47
40X-5, 21	307.7	16	53	142	24	245	26	102.0	101.9	99.1	101.0	1.00	1.03	1.03	64
41X-1, 27	310.8	37	10	133	31	291	57	135.5	133.8	132.7	134.0	1.01	1.01	1.02	33
41X-2, 136	313.4	300	5	37	54	207	35	111.6	110.5	107.8	110.0	1.01	1.02	1.04	55
41X-4, 23	315.2	82	5	350	9	203	80	123.5	122.6	119.9	122.0	1.01	1.02	1.03	10
146-889B															
4R-3, 3	227.8	238	30	123	36	356	40	119.4	118.0	116.5	118.0	1.01	1.01	1.02	51
6R-1, 37	244.7	344	24	245	20	120	58	70.3	70.1	69.6	70.0	1.00	1.01	1.01	32
7R-4, 42	257.7	321	24	55	7	160	65	148.8	147.9	147.2	148.0	1.01	1.00	1.01	26
8R-1, 88	263.6	97	49	284	41	190	4	302.7	297.5	293.8	298.0	1.02	1.01	1.03	86
8R-4, 19	267.4	91	16	196	43	345	42	183.4	179.3	177.2	180.0	1.02	1.01	1.04	48
9R-1, 72	272.3	106	26	219	40	353	39	90.5	90.2	89.2	90.0	1.00	1.01	1.01	51
10R-2, 97	282.9	68	15	273	74	159	7	286.4	284.5	281.2	284.0	1.01	1.01	1.02	83
12R-1, 71	298.9	341	33	218	40	96	33	138.0	137.8	135.2	137.0	1.00	1.02	1.02	57
13R-3, 60	310.5	280	1	11	19	187	71	132.5	131.9	131.6	132.0	1.00	1.00	1.01	19
15R-1, 122	325.8	183	35	324	49	79	20	123.7	123.1	122.1	123.0	1.00	1.01	1.01	70
17R-1, 113	343.2	62	11	231	79	331	2	137.4	136.9	133.7	136.0	1.00	1.02	1.03	88
146-889D															
3X-1, 60	140.6	179	51	279	8	15	38	89.1	88.6	86.3	88.0	1.00	1.03	1.03	52
4N-1, 88	150.4	179	35	86	4	350	54	282.8	279.6	274.6	279.0	1.01	1.02	1.03	36
4N-2, 10	151.1	64	12	154	6	268	76	155.9	154.9	148.2	153.0	1.01	1.05	1.05	14
146-890B															
1H-1, 10	0.1	141	73	307	17	39	4	714.2	711.6	701.1	709.0	1.00	1.02	1.02	86
1H-1, 132	1.3	64	62	197	20	294	19	1046.7	1041.6	1010.6	1033.0	1.00	1.03	1.04	71
1H-5, 59	6.6	304	5	36	10	190	79	979.7	968.3	937.9	962.0	1.01	1.03	1.04	11
2H-2, 84	9.7	84	6	353	2	248	84	1431.8	1416.3	1249.7	1365.9	1.01	1.13	1.15	6
2H-5, 90	14.4	306	31	216	1	124	59	1480.4	1469.8	1444.7	1465.0	1.01	1.02	1.02	32
3H-2, 64	18.9	276	1	7	12	181	78	122.4	120.8	119.8	121.0	1.01	1.01	1.02	12
3H-4, 35	21.6	139	19	232	10	348	68	1260.8	1249.6	1224.5	1245.0	1.01	1.02	1.03	22
3H-6, 81	25.1	125	5	216	18	20	72	107.9	107.4	105.8	107.0	1.01	1.02	1.02	18
5H-3, 46	41.4	71	8	181	69	338	20	108.8	108.1	107.1	108.0	1.01	1.01	1.02	70
5H-5, 74	44.4	260	16	162	25	19	59	116.3	114.6	114.1	115.0	1.02	1.00	1.02	31
5H-7, 102	47.5	88	5	182	42	352	48	215.0	208.8	200.2	208.0	1.03	1.04	1.07	42

Notes: Dec = declination (degrees); Inc = inclination (degrees); K_{max}, K_{int}, K_{min}, K_{mean} in SI volume units; $L = K_{max}/K_{int}$; $F = K_{int}/K_{min}$; $P = K_{max}/K_{min}$; AMS dip = (90–K_{min} inc).

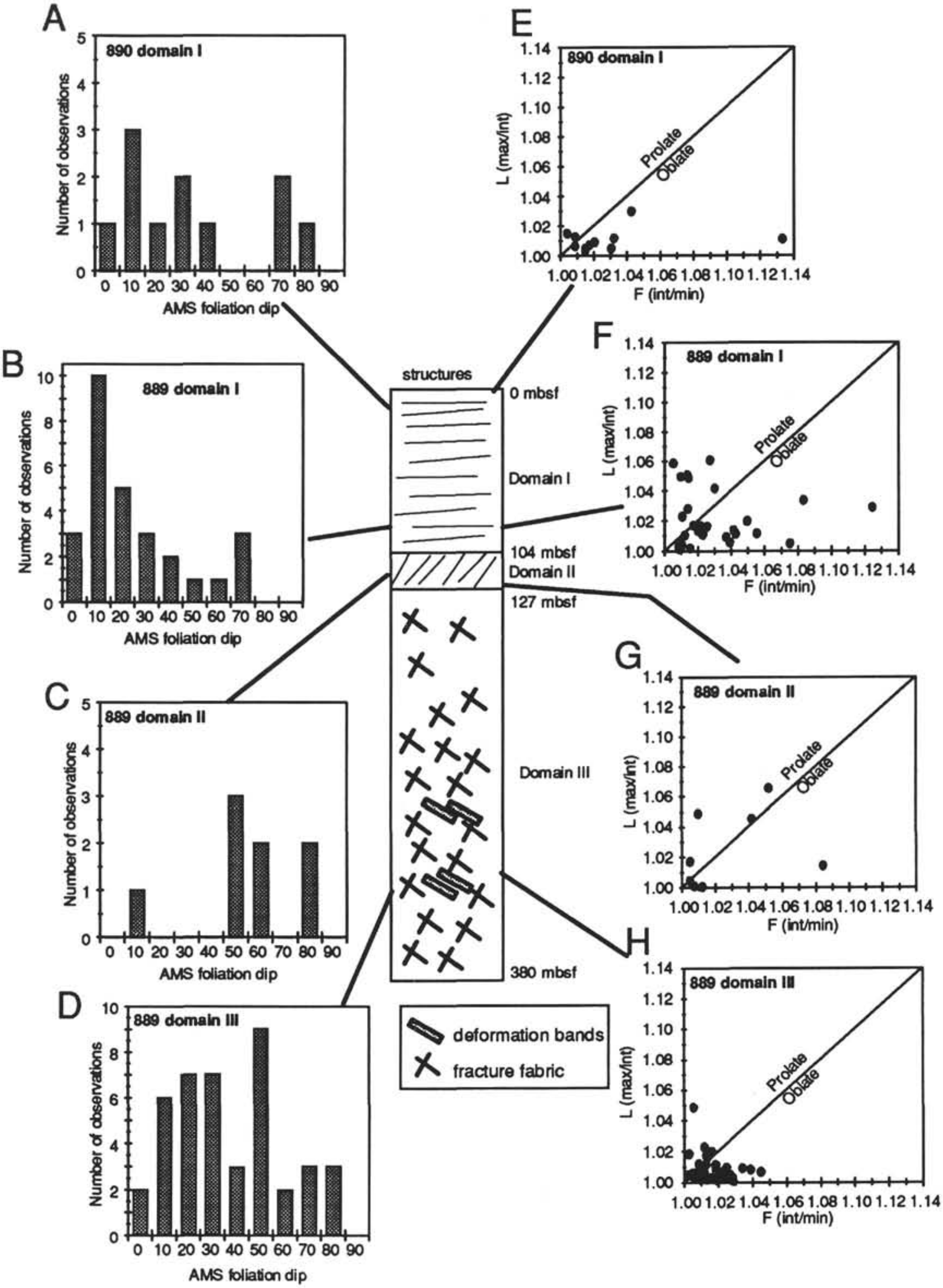

Figure 8. AMS results and schematic column of the principal structures (bedding, fracture fabrics, and deformation bands) and boundaries of the structural domains of Site 889/890. **A–D.** The orientations of the AMS fabrics are plotted as histograms of AMS foliation dips for each structural domain. The AMS foliation dips are defined as 90° (inclination of the minimum axis) for each sample, and represent the dips of the dominant planar fabric measured by AMS in these samples. **E–H.** The shapes of the AMS ellipsoids are given as Flinn-type diagrams, as in Figure 5.

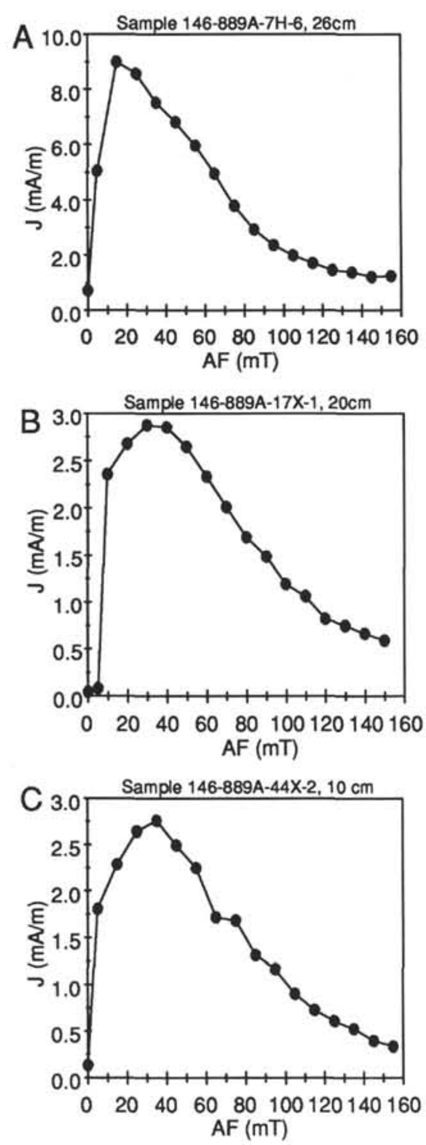

Figure 9. pARM curves for representative Site 889/890 samples. The vertical axis are magnetization (mA/m), and the horizontal axes are the intensities of the alternating field used to generate the pARM for each step. A 10-mT-wide window was used, and the center of the window was marked in increments of 10 mT from 5 to 155 mT. All samples have peak pARMs between 15 mT and 35 mT, with most of the pARM occurring between 5 and 60 mT.

13B). The highest concentration of AMS foliation dips occurs between 40° and 50°, which agrees well with the orientations of the fracture fabrics in this domain. The shapes of the AMS el psoids are with few exceptions oblate and moderately anisotropic (g. 13G). The AMS foliations in structural domain III dip between 20° and 60°, which is similar to the dips of the fissility fabrics which characterize this interval (Fig. 13C). The shapes of the AMS ellipsoids in this domain vary between moderately prolate to oblate (Fig. 13H). In structural domain IV the AMS foliations dip predominantly between 30° and 70° (Fig. 13D), which, like domain II, agrees well with the measured dips of the fracture fabrics in this domain. The shapes of the AMS ellipsoids in domain IV are almost all moderately oblate (Fig. 13I). In structural domain V the distribution of the AMS foliation dips has two peaks (one between 5° and 40°, the other between 50° and 70°; Fig. 13E). The steeper AMS foliation dips occur in the upper portion of domain V (from 383 to 446 mbsf); below 446 mbsf all of the AMS foliation dips are shallow. The steeply dipping AMS fabrics occur near deformation bands, and may also be the result of a postulated fault between 410 and 446 mbsf (Westbrook, Carson, Musgrave, et al., 1994). The shapes of the AMS ellipsoids in domain V are mostly oblate (Fig. 13J). One specimen, which was taken near a deformation band in Core 146-891B-55X, has a prolate AMS ellipsoid.

Site 892

Site 892 was drilled through a thrust fault in the upper portion of the Cascadia accretionary prism to the E-NE of Site 891 (Fig. 1). The lithology of the drilled interval is clayey silt and silty clay. Based on shipboard observations, three structural domains were defined at this site (Westbrook, Carson, Musgrave, et al., 1994). Structural domain I (0 to 52 mbsf) was defined primarily by a change in bedding dips from 20°–36° above 52 mbsf to dips less than 20° below 52 mbsf in Hole 892A. Bedding dips in Hole 892D are shallow (less than 20°), and do not vary across the boundary at 52 mbsf. A reversal in biostratigraphic ages occurs near 52 mbsf, which, combined with the variation in dips in Hole 892A, indicates the presence of a thrust fault at this depth (Westbrook, Carson, Musgrave, et al., 1994). Structural domain II (52–110 mbsf) is marked by shallow (10° to 20°) bedding dips and a weak, steeply dipping fracture fabric. Domain III (110 to 170 mbsf) is characterized by the occurrence of well-developed stratal disruption and mélange fabrics. The mélange fabrics dip between 10° and 20°.

A wide variation in the relative contributions of paramagnetic clays and ferrimagnetic minerals in the Site 892 specimens is found by comparison between the high-field and low-field susceptibilities (Fig. 14). The contribution of the paramagnetic minerals to the low-field susceptibility (k_{HF}/k_{LF}) varies from 20% to 80%. The AMS results from this site will thus represent composite magnetic fabrics, such as were found in the Site 889/890 specimens. Like the Site 889/890 specimens, the paramagnetic susceptibility is relatively constant at Site 892, so the variation in k_{HF}/k_{LF} can be attributed to variations in the amount and species of the ferrimagnetic minerals. In the mIRM experiments the low coercivity (0.05 T) component carried the majority of the mIRM, and as at the previous site, two thermal unblocking temperatures (310° C and between 550° and 590°C) were observed (Fig. 15). These mIRM results, along with the reducing pore water chemistry (Westbrook, Carson, Musgrave, et al., 1994) indicate the presence of both magnetic sulfides (greigite and/or pyrrhotite) and magnetite in most of the specimens.

Despite the variations in susceptibility carriers in the specimens from Site 892, the AMS results are fairly consistent with the observed structures (Table 5). In structural domain I, the majority of the specimens have AMS foliations dipping less than 40° (Fig. 16A). Unlike the measured bedding, there is no noticeable difference between foliation dips from Holes 892A and 892D. Susceptibility ellipsoid shapes from most of the specimens in domain I are weakly oblate (Fig. 16D). The AMS fabrics of specimens from structural domain II are similar to those of domain I. The AMS foliations have dips strongly concentrated between 10° and 40° (Fig. 16B). Like domain I, the shapes of the AMS ellipsoids are weakly oblate for most of the specimens from domain II (Fig. 16E). In structural domain III the mélange fabrics are well-recorded by the AMS results. The concentration of dips from 10° to 20° occur in specimens from the well-developed mélange fabrics (Fig. 16C). The steeper (20° to 40°) dips are in specimens without well-developed mélange fabrics, and agree with bedding orientations in this domain. The shapes of the susceptibility ellipsoids in domain III are oblate and more anisotropic than those of domains I and II (Fig. 16F).

Measurements of ARMA were made on specimens from Site 892 to avoid some of the effects of variations in susceptibility carriers on the magnetic fabrics. The pARM results for this site have peaks between 25 and 40 mT (Fig. 17), and from these results an alternating field window from 5 to 60 mT was selected for the ARMA experiments. The ARMA results (Table 6) are very well-clustered. In do-

Table 3. Anhysteretic remanent magnetization anistropy (ARMA) data for Site 889/890.

Core, section, interval (cm)	Depth (mbsf)	$pARM_{max}$		$pARM_{int}$		$pARM_{min}$		pARM (mA/m)				L	F	P	ARMA dip
		Dec	Inc	Dec	Inc	Dec	Inc	Max	Int	Min	Mean				
146-889A-															
1H-1, 84	20.8	177	4	87	2	327	86	428.3	424.5	374.4	409.1	1.01	1.13	1.14	4
2H-5, 103	36.5	121	27	216	10	325	61	534.9	527.4	505.0	522.5	1.01	1.04	1.06	29
3H-2, 21	39.7	133	15	224	2	323	75	284.5	275.1	263.8	274.5	1.03	1.04	1.08	15
4H-4, 81	52.7	136	13	39	27	249	60	477.8	452.0	416.9	448.9	1.06	1.08	1.15	30
5H-3, 92	61.9	174	1	264	9	75	81	22.2	20.9	20.2	21.1	1.06	1.03	1.10	9
6H-2, 68	68.8	153	16	57	20	279	63	75.8	73.0	64.3	71.0	1.04	1.14	1.18	27
7H-2, 58	79.1	322	7	222	57	56	32	17.9	17.2	17.1	17.4	1.04	1.01	1.05	58
7H-6, 26	83.8	271	59	5	2	97	31	41.4	38.5	35.1	38.3	1.08	1.10	1.18	59
8H-3, 9	89.6	5	21	258	37	119	46	26.6	24.2	20.8	23.9	1.10	1.17	1.28	44
10H-1, 91	104.9	185	62	311	18	49	22	145.0	138.4	128.2	137.2	1.05	1.08	1.13	68
10H-6, 63	111.9	342	51	165	39	74	1	76.0	74.7	71.7	74.1	1.02	1.04	1.06	89
11H-1, 33	113.8	123	3	27	66	214	24	264.6	252.8	230.1	249.2	1.05	1.10	1.15	66
11H-4, 39	118.4	339	30	122	54	238	18	175.6	171.4	164.3	170.4	1.02	1.04	1.07	72
17X-1, 20	130.3	325	45	88	29	198	31	14.3	13.6	13.3	13.7	1.05	1.03	1.08	59
18X-6, 55	146.6	295	21	198	19	69	61	45.7	45.3	43.4	44.8	1.01	1.04	1.05	29
25X-1, 53	197.8	104	1	13	9	202	81	27.6	27.1	26.5	27.1	1.02	1.02	1.04	9
26X-2, 39	208.7	170	12	76	19	291	68	10.8	9.7	9.5	10.0	1.11	1.03	1.14	22
28X-5, 24	223.1	4	1	273	45	95	45	23.6	23.3	22.2	23.0	1.01	1.05	1.06	45
34X-3, 48	260.7	217	26	312	9.3	60	62	24.7	23.8	22.5	23.7	1.04	1.06	1.10	28
41X-1, 20	310.7	275	16	141	67	10	15	15.0	14.9	14.8	14.9	1.00	1.01	1.02	75
41X-2, 122	313.2	248	4.6	340	14	141	75	12.0	11.6	11.1	11.6	1.03	1.04	1.07	15
41X-4, 40	315.4	287	3.4	20	43	193	47	18.7	18.3	17.4	18.1	1.03	1.05	1.08	43
44X-2, 10	338.3	315	5	48	29	217	61	13.8	13.5	12.9	13.4	1.02	1.05	1.07	29
146-889B-															
4R-3, 15	227.8	44	23	306	18	181	60	59.3	44.8	33.6	45.9	1.32	1.33	1.76	30
8R-1, 65	263.4	10	0	280	60	100	30	47.4	46.2	45.2	46.3	1.03	1.02	1.05	60
146-889D-															
4N-1, 41	149.9	323	5	53	5	185	83	21.4	20.4	19.1	20.3	1.05	1.07	1.12	7

Notes: Dec = declination (degrees); Inc = inclination (degrees); Max, Int, Min, Mean = pARM in mA/m; L = max/int; F = int/min; P = max/min; ARMA dip = (90 – $pARM_{min}$ inc).

main I, all ARMA dips are less than 30° (Fig. 18A) with triaxial to weakly oblate ellipsoid shapes (Fig. 18D). In structural domain II, the ARMA foliations dip less than 30° (Fig. 18B), and have either oblate or triaxial ellipsoid shapes (Fig. 18E). The ARMA fabrics from structural domain III have dips between 10° and 30° (Fig. 18C). The ARMA orientation of Specimen 146-892A-18X-1, 72 cm (145.3 mbsf) exactly matches the orientation of deformation bands in this interval measured while at sea. The shapes of the ARMA ellipsoids from this domain are moderately anisotropic and oblate (Fig. 18F).

DISCUSSION

Accretionary prisms are ideally suited for the use of magnetic fabrics as strain markers, as the low temperatures during deformation and high porosities of the accreting sediments will be most likely to develop mineral preferred orientations via grain rotation rather than pressure solution (Maltman, 1984). Grain rotation would allow the use of either passive line (March) or rigid marker solutions to numerical models correlating magnetic anisotropy and finite strain (Owens, 1974; Richter, 1992). Magnetic anisotropy can only be used as a proxy for finite strains in these models when a single mineral controls the measured magnetic fabric (Borradaile, 1991; Richter, 1992). Because the specimens from the Cascadia accretionary prism all have mixed contributions of either paramagnetic clays and ferrimagnetic minerals, or of two types of ferrimagnetic minerals, to the measured magnetic anisotropy fabrics, finite strains cannot be calculated from the results of this study. This conclusion clearly demonstrates the need for careful rock magnetic studies in conjunction with magnetic anisotropy work. More detailed rock magnetic techniques, such as measurement of the anisotropy of high-field (paramagnetic) susceptibility, or of low-temperature susceptibility (e.g., Richter and van der Pluijm, 1994) are needed to extract a single-mineral dominated magnetic fabric from these specimens.

This study has shown, despite the complications introduced by the composite magnetic fabrics, that magnetic anisotropy fabrics agree well with observed structures in weakly deformed accretionary prism sediments. At the very least magnetic anisotropy measurements can serve to augment the available structural data, which will aid interpretations of the structural geology of these sites. A more detailed comparison is possible between two of the sites (888 and 891) that have similar magnetic susceptibility carriers. In both of these sites, greater than 90% of the low-field susceptibility is carried by ferrimagnetic minerals (Figs. 3 and 11). Both magnetite and magnetic sulfides (greigite and pyrrhotite) are present in similar (relative) proportions in specimens from both sites (compare Figs. 4 and 12). Site 891 was interpreted to have been deposited in a submarine fan environment (Westbrook, Carson, Musgrave, et al., 1994) similar to that of Site 888. Both sites have similar lithologies, were deposited with rapid sedimentation rates, and are of similar (<780 ka) age. These similarities suggest that the AMS fabrics at Site 888 can serve as a sedimentary-fabric reference for the AMS fabrics measured in the deformed sediments of Site 891. The AMS fabrics from most of the Site 888 specimens are nearly uniaxial-oblate, and vary in degree of anisotropy from P (k_{max}/k_{min}) = 1.03 to 1.26. The AMS fabrics from Site 891 have a slightly lower degree of anisotropy, ranging from P = 1.03 to 1.16. The shapes of the AMS ellipsoids from Site 891 range from uniaxial-oblate, to triaxial shapes, to prolate. Most of the specimens from Site 891 with prolate ellipsoid shapes are from specimens near deformation bands or in intervals near faults (e.g., Cores 146-891B-23X and 146-891B-41X). The shift of the Site 891 AMS ellipsoid specimens to less-anisotropic, and, especially, to prolate shapes, indicates that significant modification of the mineral fabrics in these sediments has occurred. The overall reduction in degree of anisotropy at Site 891 is consistent with a weakly developed, horizontal-compression fabric superimposed on an initial bedding fabric (shallowly dipping, uniaxial-oblate). Similar modification of magnetic anisotropy fabrics by imposition of sub-horizontal compression on an initially oblate (vertical compaction) fabric in accretionary prism sediments was found in the Nankai prism (Byrne et al., 1993), and is consistent with AMS data from the Barbados accretionary prism as well (Hounslow, 1990). Magnetic anisotropy results thus suggest the occurrence of a weakly developed mineral fabric resulting from tectonic strains in the Site 891 specimens.

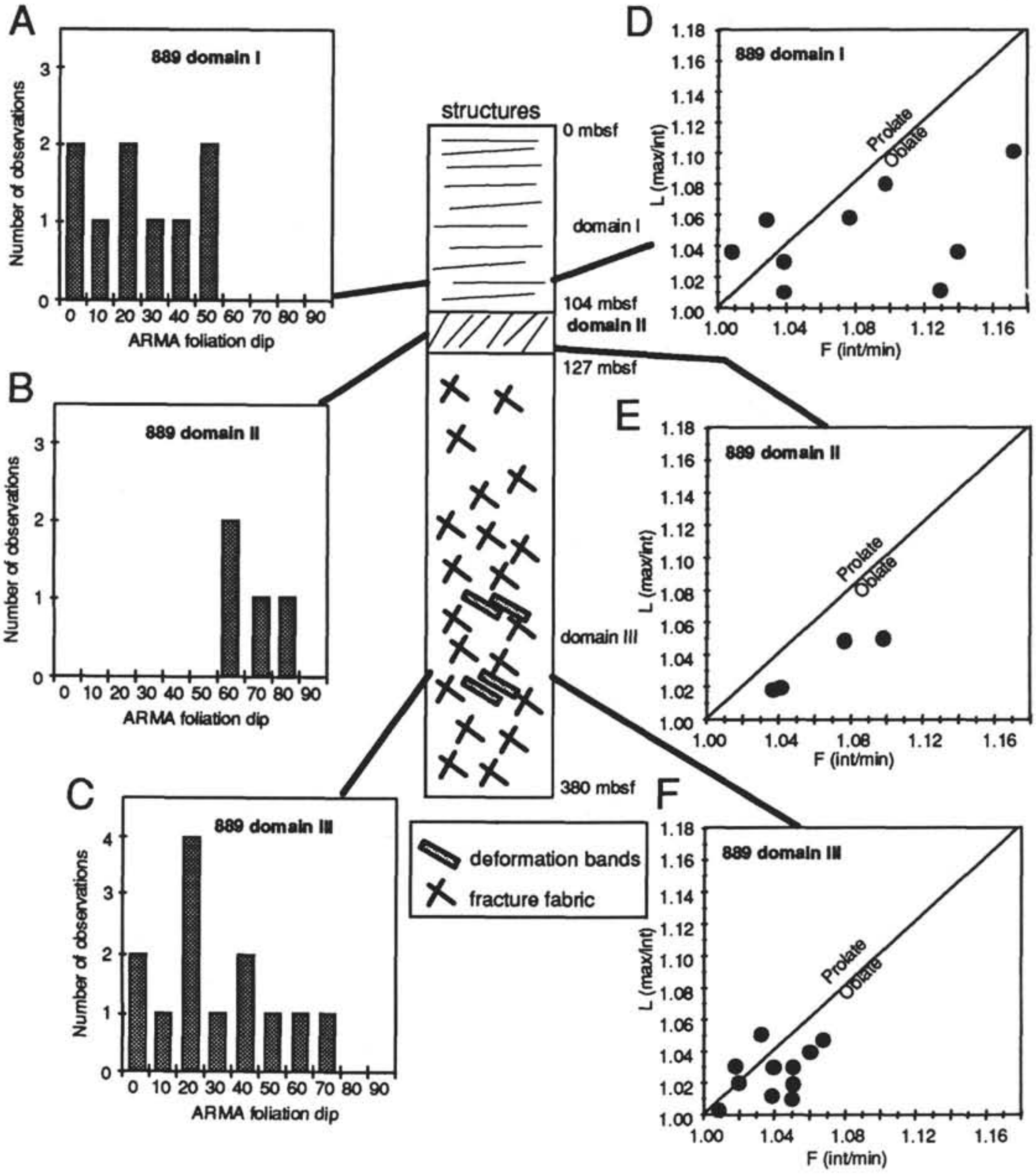

Figure 10. ARMA results for Site 889/890 samples. The ARMA orientations (**A–C**) and ellipsoid shapes (**D–F**) are plotted for each structural domain as in Figure 8.

ACKNOWLEDGMENTS

B. Housen thanks JOI/USSAC and B. van der Pluijm (NSF grant EAR-91-19196) for funding this research, and the NSF, Keck Foundation, and University of Minnesota for funding two visits to the Institute for Rock Magnetism. Subir Banerjee, Chris Hunt, Jim Marvin and Bruce Moscowitz are thanked for their help and comments while at the *IRM*. T. Sato thanks E. Herrero-Bervera (Hawaii Institute for Geophysics) and M. Torii (Kyoto University) for assistance while using their laboratories. Carl Richter and Ken Kodama are thanked for their helpful reviews of this manuscript. Ben van der Pluijm, John Stamatakos, Rob Van der Voo, Bob Musgrave, Harold Tobin and Casey Moore are thanked for their various comments during this project.

REFERENCES

Borradaile, G.J., 1991. Correlation of strain with anisotropy of magnetic susceptibility (AMS). *Pure Appl. Geophys.,* 135:15–29.

Borradaile, G.J., Keeler, W., Alford, C., and Sarvas, P., 1987. Anisotropy of magnetic susceptibility of some metamorphic minerals. *Phys. Earth Planet. Inter.,* 48:161–166.

Byrne, T., Brückmann, W., Owens, W., Lallemant, S., and Maltman, A., 1993. Structural synthesis: correlation of structural fabrics, velocity anisotropy, and magnetic susceptibility data. *In* Hill, I.A., Taira, A., Firth, J.V., et al., *Proc. ODP, Sci. Results,* 131: College Station, TX (Ocean Drilling Program), 365–378.

Girdler, R.W., 1961. The measurement and computation of anisotropy of magnetic susceptibility of rocks. *Geophys. J. R. Astron. Soc.,* 5:34–44.

Hounslow, M.W., 1990. Grain fabric measured using magnetic susceptibility anisotropy in deformed sediments of the Barbados Accretionary Prism:

Leg 110. *In* Moore, J.C., Mascle, A., et al., *Proc. ODP, Sci. Results,* 110: College Station, TX (Ocean Drilling Program), 257–275.
Housen, B.A., Richter, C., and van der Pluijm, B.A., 1993. Composite magnetic anisotropy fabrics: experiments, numerical models, and implications for the quantification of rock fabrics. *Tectonophysics,* 220:1–12.
Jackson, M., Gruber, W., Marvin J., and Banerjee, S.K., 1988. Partial anhysteretic remanence and its anisotropy: applications and grainsize-dependence. *Geophys. Res. Lett.,* 15:440–443.
Lowrie, W., 1990. Identification of ferromagnetic minerals in a rock by coercivity and unblocking temperature properties. *Geophys. Res. Lett.,* 17:159–162.
Maltman, A., 1984. On the term "soft-sediment deformation." *J. Struct. Geol.,* 6:589–592.
McCabe, C., Jackson, M., and Ellwood, B.B., 1985. Magnetic anisotropy in the Trenton Limestone: results of a new technique, anisotropy of anhysteretic susceptibility. *Geophys. Res. Lett.,* 12:333–336.
Owens, W.H., 1974. Mathematical model studies on factors affecting the magnetic anisotropy of deformed rocks. *Tectonophysics,* 24:115–131.
————, 1993. Magnetic fabric studies of samples from Hole 808C, Nankai Trough. *In* Hill, I.A., Taira, A., Firth, J.V., et al., *Proc. ODP, Sci. Results,* 131: College Station, TX (Ocean Drilling Program), 301–310.
Potter, D.K., and Stephenson, A., 1988. Single-domain particles in rocks and magnetic fabric analysis. *Geophys. Res. Lett.,* 15:1097–1100.
Richter, C., 1992. Particle motion and the modelling of strain response in magnetic fabrics. *Geophys. J. Int.,* 110:451–464.
Richter, C., and van der Pluijm, B.A., 1994. Separation of paramagnetic and ferrimagnetic susceptibilities using low temperature magnetic susceptibilities and comparison with high field methods. *Phys. Earth Planet. Inter.,* 82:113–123.
Rochette, P., 1987. Magnetic susceptibility of the rock matrix related to magnetic fabric studies. *J. Struct. Geol.,* 9:1015–1020.
Westbrook, G.K., Carson, B., Musgrave, R.J., et al., 1994. *Proc. ODP, Init. Repts.,* 146 (Pt. 1): College Station, TX (Ocean Drilling Program).

Date of initial receipt: 2 September 1994
Date of acceptance: 9 March 1995
Ms 146SR-217

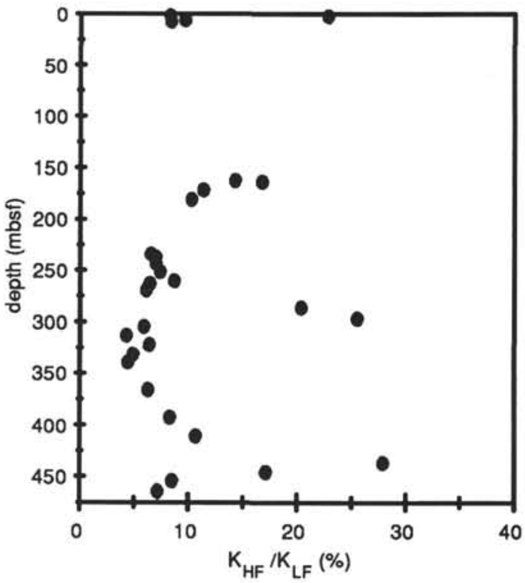

Figure 11. Depth (mbsf) vs. the percentage of low-field magnetic susceptibility carried by the paramagnetic minerals in sediments from Site 891, as determined by comparing the high-field and low-field susceptibilities. Here, the majority (>90%) of the low-field susceptibility is carried by the ferrimagnetic minerals, with the exception of two horizons (one at 280–290 mbsf, the other at 430–440 mbsf) that have higher paramagnetic contributions.

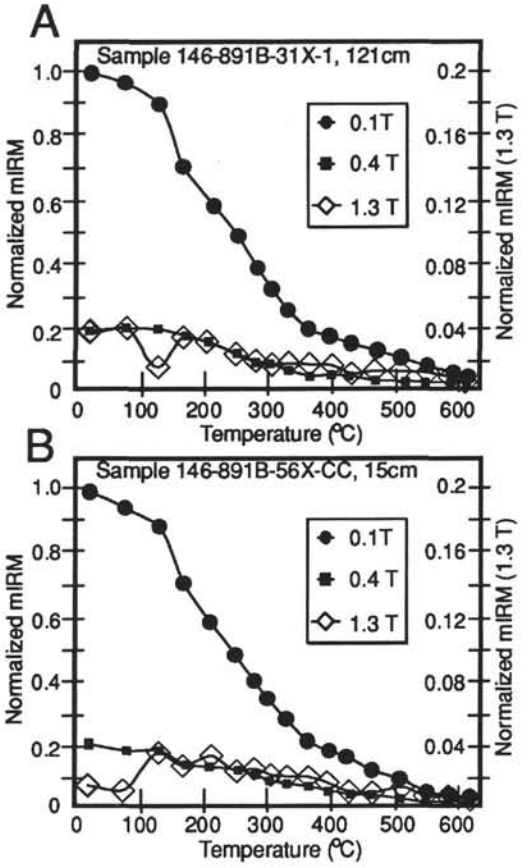

Figure 12. Thermal demagnetization of mIRM results from two representative samples from Site 891. The left vertical axis is normalized magnetization of the 0.1 T and 0.4 T mIRM components, and the right vertical axis is the normalized intensity of the 1.4 T mIRM component. The horizontal axis is the temperature of the thermal demagnetization step (°C). In all Site 891 samples the 0.1 T component carries most of the mIRM, and two thermal unblocking temperatures (T_{ub}), (one at about 300° to 350°C, and the other at about 580°C) are observed. This indicates that both greigite and/or pyrrhotite (T_{ub} ~300°C) and magnetite (T_{ub} ~580°C) are the dominant magnetic minerals in these sediments.

Table 4. Anisotropy of magnetic susceptibility (AMS) data for Site 891.

Core, section, interval (cm)	Depth (mbsf)	K_{max} Dec	K_{max} Inc	K_{int} Dec	K_{int} Inc	K_{min} Dec	K_{min} Inc	K_{max} (1×10^{-6})	K_{int} (1×10^{-6})	K_{min} (1×10^{-6})	K_{mean} (1×10^{-6})	L	F	P	AMS dip
146-891A-															
1H-2, 89	2.4	210	36	71	46	317	21	857.1	842.7	796.1	832.0	1.02	1.06	1.08	69
1H-2, 123	2.7	140	42	29	22	278	40	557.8	538.4	493.8	530.0	1.04	1.09	1.13	50
1H-2, 136	2.9	167	62	67	6	333	27	245.4	231.7	224.9	234.0	1.06	1.03	1.09	63
1H-3, 14	3.1	214	40	69	44	320	19	2355.7	2329.9	2280.3	2322.0	1.01	1.02	1.03	72
1H-3, 47	3.5	286	14	67	72	193	11	83.8	83.6	81.5	83.0	1.00	1.03	1.03	79
2H-1, 5	4.8	201	38	82	32	325	36	722.1	675	657	684.7	1.07	1.03	1.10	54
2H-1, 68	5.4	108	85	204	1	294	5	865.8	837.8	792.3	832.0	1.03	1.06	1.09	85
2H-1, 100	5.7	18	27	174	60	283	11	1406.1	1388	1237.9	1344.0	1.01	1.12	1.14	79
2H-2, 38	6.3	232	65	8	19	103	17	837.0	793.1	772.8	801.0	1.06	1.03	1.08	73
3H-1, 21	7.5	127	38	325	51	224	8.8	1496	1467.5	1410.6	1458.0	1.02	1.04	1.06	81
3H-1, 27	7.6	254	45	70	45	162	2	1034.8	996.6	944.5	992.0	1.04	1.06	1.10	88
146-891B-															
14X-1, 76	110.3	83	17	183		328	55	1735.8	1697.6	1570.6	1668.0	1.02	1.08	1.11	35
15X-1, 12	118.5	71	47	186	22	293	35	2512.1	2433.4	2359.5	2435.0	1.03	1.03	1.06	55
16X-1, 10	127.4	24	40	166	44	277	20	1423.6	1371	1303.4	1366.0	1.04	1.05	1.09	70
19X-1, 54	154.4	85	37	179	5	276	53	1471.8	1422.7	1350.5	1415.0	1.03	1.05	1.09	37
20X-1, 2	162.7	56	55	167	15	266	31	687.4	678.2	638.3	668.0	1.01	1.06	1.08	60
20X-1, 13	162.8	175	7	84	7	311	80	790.3	764.7	760.9	772.0	1.03	1.00	1.04	10
20X-1, 56	163.3	292	51	122	39	29	5	963.8	925.0	901.2	930.0	1.04	1.03	1.07	85
20X-1, 78	163.5	293	41	26	3	119	49	813.8	804.8	781.3	800.0	1.01	1.03	1.04	41
20X-1, 83	163.5	283	49	51	28	157	27	1475.3	1446	1377.8	1433.0	1.02	1.05	1.07	63
20X-1, 118	163.9	66	50	199	30	304	24	627.1	609.0	575.8	604.0	1.03	1.06	1.09	66
21N-1, 18	171.8	37	38	259	44	145	22	904.6	887.3	857.1	883.0	1.02	1.04	1.06	68
23X-1, 41	180.9	79	10	327	63	173	25	1058.0	1040.2	970.7	1023.0	1.02	1.07	1.09	65
23X-1, 90	181.4	359	65	249	9	156	23	1663.5	1572.8	1545.6	1594.0	1.06	1.02	1.08	67
23X-1, 94	181.4	121	46	233	20	339	37	2647	2501.4	2402.5	2517.0	1.06	1.04	1.10	53
23X-2, 26	182.3	58	49	230	40	323	3.8	3382.6	3215.5	3187.9	3262.0	1.05	1.01	1.06	86
26X-1, 23	207.3	46	60	259	26	162	14	3059.1	2986.6	2912.3	2986.0	1.02	1.03	1.05	76
28X-1, 23	224.9	56	45	315	11	215	43	2462.2	2432.4	2428.3	2441.0	1.01	1.00	1.01	47
28X-CC, 14	225.5	42	21	310	5	207	68	2976.8	2914.3	2742.9	2878.0	1.02	1.06	1.09	22
29X-1, 37	234.0	217	22	87	58	316	22	2417.5	2380.8	2305.6	2368.0	1.02	1.03	1.05	68
29X-1, 71	234.3	119	62	333	23	237	14	1984.3	1897.4	1761.1	1880.9	1.05	1.08	1.13	76
30X-1, 3	237.6	30	59	163	22	262	20	1568.3	1560.7	1430.8	1520.0	1.00	1.09	1.10	70
30X-1, 19	237.8	58	69	172	9	265	19	2226.2	2139.1	2120.7	2162.0	1.04	1.01	1.05	71
30X-2, 51	238.9	103	27	195	5	295	62	2610.7	2547.8	2380.5	2513.0	1.02	1.07	1.10	28
31X-1, 79	243.2	102	2	192	15	4	75	1240.8	1202.1	1124.0	1189.0	1.03	1.07	1.10	15
31X-1, 121	243.6	175	39	56	31	300	36	2469.5	2443.5	2377	2430.0	1.01	1.03	1.04	54
31X-2, 5	244.0	37	10	305	10	172	76	2218.4	2188.1	2007.5	2138.0	1.01	1.09	1.11	14
31X-CC, 15	244.2	64	15	333	1	238	75	1297.0	1270.1	1173.8	1247.0	1.02	1.08	1.10	15
32X-1, 26	251.7	121	0	211	70	31	20	1602.5	1524.0	1451.4	1526.0	1.05	1.05	1.10	70
33X-1, 26	260.5	234	18	339	38	123	47	676.4	662.8	634.1	657.8	1.02	1.05	1.07	43
33X-1, 35	260.6	253	59	346	2	78	30	1103.1	1059.5	1026.3	1063.0	1.04	1.03	1.07	60
34X-1, 35	263.5	221	50	126	4	32	39	1558.6	1522.8	1451.5	1510.9	1.02	1.05	1.07	51
34X-1, 54	263.6	19	8	112	18	267	71	2746.7	2670.2	2485.1	2634.0	1.03	1.07	1.11	19
35X-1, 46	269.5	275	2	7	47	184	43	1481.2	1470.2	1404.5	1451.9	1.01	1.05	1.05	47
35X-1, 143	270.4	301	30	46	23	166	51	1620.7	1503.6	1495.7	1540.0	1.08	1.01	1.08	40
35X-2, 5	270.6	176	41	75	13	331	46	2372.7	2330.1	2230.2	2311.0	1.02	1.04	1.06	44
35X-CC, 19	270.9	182	29	281	16	36	56	2939.2	2898.9	2762.9	2867.0	1.01	1.05	1.06	34
38X-1, 20	286.6	236	6	138	54	331	35	383.2	372.4	357.4	371.0	1.03	1.04	1.07	55
38X-1, 61	287.0	8.5	25	193	65	99	2	1709.7	1690.7	1687.7	1696.0	1.01	1.00	1.01	88
38X-2, 38	288.3	232	7	141	3	33	82	406.1	403.6	366.2	392.0	1.01	1.10	1.11	8
38X-2, 39	288.3	176	27	278	21	41	55	823.8	810.2	801	811.7	1.02	1.01	1.03	36
38X-CC, 10	289.3	328	33	203	41	81	31	871.2	839.6	791.5	834.1	1.04	1.06	1.10	59
39X-1, 138	296.5	81	45	260	45	351	0	1104.7	1048.5	1011.8	1055.0	1.05	1.04	1.09	90
39X-CC, 28	297.2	181	29	272	2	6	61	361.4	343.4	318.2	341.0	1.05	1.08	1.14	29
39X-CC, 35	297.3	190	27	283	6	26	63	446.8	425.4	407.2	426.5	1.05	1.04	1.10	27
40X-1, 41	304.4	117	31	214	12	323	56	1045.9	1037.1	962.0	1015.0	1.01	1.08	1.09	34
40X-1, 103	305.0	104	33	2	18	248	51	1151.0	1118.3	1099.7	1123.0	1.03	1.02	1.05	39
40X-2, 30	305.8	244	43	154	10	65	47	481.1	476.0	443.9	467.0	1.01	1.07	1.08	43
40X-2, 38	305.9	120	13	216	22	3	64	954.9	921.3	824.4	900.2	1.04	1.12	1.16	26
41X-1, 70	313.5	52	30	144	5	242	60	2863.9	2759.2	2665.9	2763.0	1.04	1.03	1.07	30
41X-1, 80	313.6	103	52	200	6	295	37	2126.5	2038.4	2018.0	2061.0	1.04	1.01	1.05	53
41X-1, 85	313.7	30	39	259	39	145	28	2259.8	2178.6	2146.5	2195.0	1.04	1.01	1.05	63
41X-2, 49	314.8	155	34	266	29	26	43	2369.9	2357.9	2247.2	2325.0	1.01	1.05	1.05	48
42X-1, 95	322.6	276	38	20	17	129	47	1468.5	1414.0	1338.3	1407.0	1.04	1.06	1.10	43
43X-2, 142	332.1	75	58	197	19	296	25	2073.6	1966.7	1929.5	1989.9	1.05	1.02	1.07	65
43X-2, 146	332.1	171	27	74	15	317	59	2546.2	2524.2	2285.6	2452.0	1.01	1.10	1.11	31
43X-3, 4	332.2	152	10	61	9	291	77	2879.1	2869.0	2688.0	2812.0	1.00	1.07	1.07	13
43X-3, 12	332.3	284	17	20	15	148	67	1719.9	1664.2	1595.7	1659.9	1.03	1.04	1.08	23
44X-1, 7	339.4	60	49	310	17	207	36	2078.5	2049.9	1871.6	2000.0	1.01	1.10	1.11	54
44X-1, 27	339.6	244	48	117	29	10	28	2851.7	2824.9	2675.2	2783.9	1.01	1.06	1.07	62
45X-1, 23	348.4	121	44	227	16	332	42	2453.6	2424.1	2169.4	2349.0	1.01	1.12	1.13	49
45X-1, 35	348.6	195	5	309	78	104	11	1307.0	1285.9	1244.0	1279.0	1.02	1.03	1.05	79
47X-1, 23	366.3	21	51	121	9	218	37	1838.2	1803.2	1713.4	1784.9	1.02	1.05	1.07	53
47X-1, 39	366.5	115	32	209	6	309	57	2196.3	2128.3	2092.3	2139.0	1.03	1.02	1.05	33
47X-2, 28	367.7	62	36	329	4	234	54	2498.6	2416.5	2314.9	2410.0	1.03	1.04	1.08	36
47X-2, 74	368.2	131	21	230	22	2	59	2253.1	2187.9	2119.9	2186.9	1.03	1.03	1.06	31
50X-1, 34	393.1	124	54	244	20	346	29	1493.4	1442.2	1378.3	1437.9	1.04	1.05	1.08	61
52X-1, 59	411.1	125	49	241	21	345	34	2108.6	2069.5	1902.9	2027.0	1.02	1.09	1.11	56
52X-1, 84	411.3	52	7	143	12	293	76	1043.0	1013.3	973.5	1010.0	1.03	1.04	1.07	14
55X-1, 24	437.2	128	30	37	3	302	60	490.4	475	468.9	478.1	1.03	1.01	1.05	30
55X-1, 29	437.3	62	29	151	1	242	61	276.4	272.3	261.3	270.0	1.01	1.04	1.06	29
55X-2, 36	438.0	187	58	59	21	319	22	358.2	351.5	343.2	351.0	1.02	1.02	1.04	68
55X-2, 58	438.3	254	19	156	21	22	61	610.4	601.5	562.9	591.6	1.01	1.07	1.08	29
55X-3, 69	439.9	75	1	345	0	230	89	479.8	473	454.8	469.2	1.01	1.04	1.05	1

Table 4. (Continued.)

Core, section, interval (cm)	Depth (mbsf)	K_{max}		K_{int}		K_{min}		K_{max} (1×10^{-6})	K_{int} (1×10^{-6})	K_{min} (1×10^{-6})	K_{mean} (1×10^{-6})	L	F	P	AMS dip
		Dec	Inc	Dec	Inc	Dec	Inc								
55X-3, 72	439.9	146	9	238	10	15	77	363.7	358.2	319.1	347.0	1.02	1.12	1.14	13
56X-1, 29	446.1	141	47	32	18	287	37	538.3	526.3	486.4	517.0	1.02	1.08	1.11	53
56X-1, 36	446.2	351	19	241	45	97	39	355.3	346.4	328.5	343.4	1.03	1.05	1.08	51
56X-2, 33	447.0	244	23	151	7	44	66	389.6	380.3	364	378.0	1.02	1.04	1.07	24
56X-2, 41	447.1	199	31	101	13	352	56	333.3	324.7	314.0	324.0	1.03	1.03	1.06	35
56X-CC, 15	447.7	120	35	233	29	352	41	971.6	957	919.5	949.4	1.02	1.04	1.06	49
57X-1, 10	454.8	92	0	2	2	191	88	1040.7	995.1	940.1	992.0	1.05	1.06	1.11	2
57X-1, 33	455.0	277	14	186	3	86	76	1723.3	1687.4	1506.3	1639.0	1.02	1.12	1.14	14
58X-1, 27	463.8	87	18	182	15	310	66	1612.5	1522.9	1442.6	1526.0	1.06	1.06	1.12	24
58X-2, 29	464.8	4	13	101	28	251	58	1299.8	1231.8	1167.4	1233.0	1.06	1.06	1.11	32
58X-2, 77	465.2	92	10	359	13	218	74	1087.5	1044.6	972.9	1035.0	1.04	1.07	1.12	16
58X-2, 82	465.3	62	23	160	18	284	61	2614.3	2576.6	2447.1	2546.0	1.01	1.05	1.07	29
58X-CC, 4	465.4	90	15	181	3	281	75	2221.2	2217.8	2022.9	2154.0	1.00	1.10	1.10	15
58X-CC, 6	465.4	262	13	171	3	68	77	1513.9	1502.6	1411.4	1476.0	1.01	1.06	1.07	13

Notes: Dec = declination (degrees); Inc = inclination (degrees); K_{max}, K_{int}, K_{min}, K_{mean} in SI volume units; $L = K_{max}/K_{int}$; $F = K_{int}/K_{min}$; $P = K_{max}/K_{min}$; AMS dip = (90 – K_{min} inc).

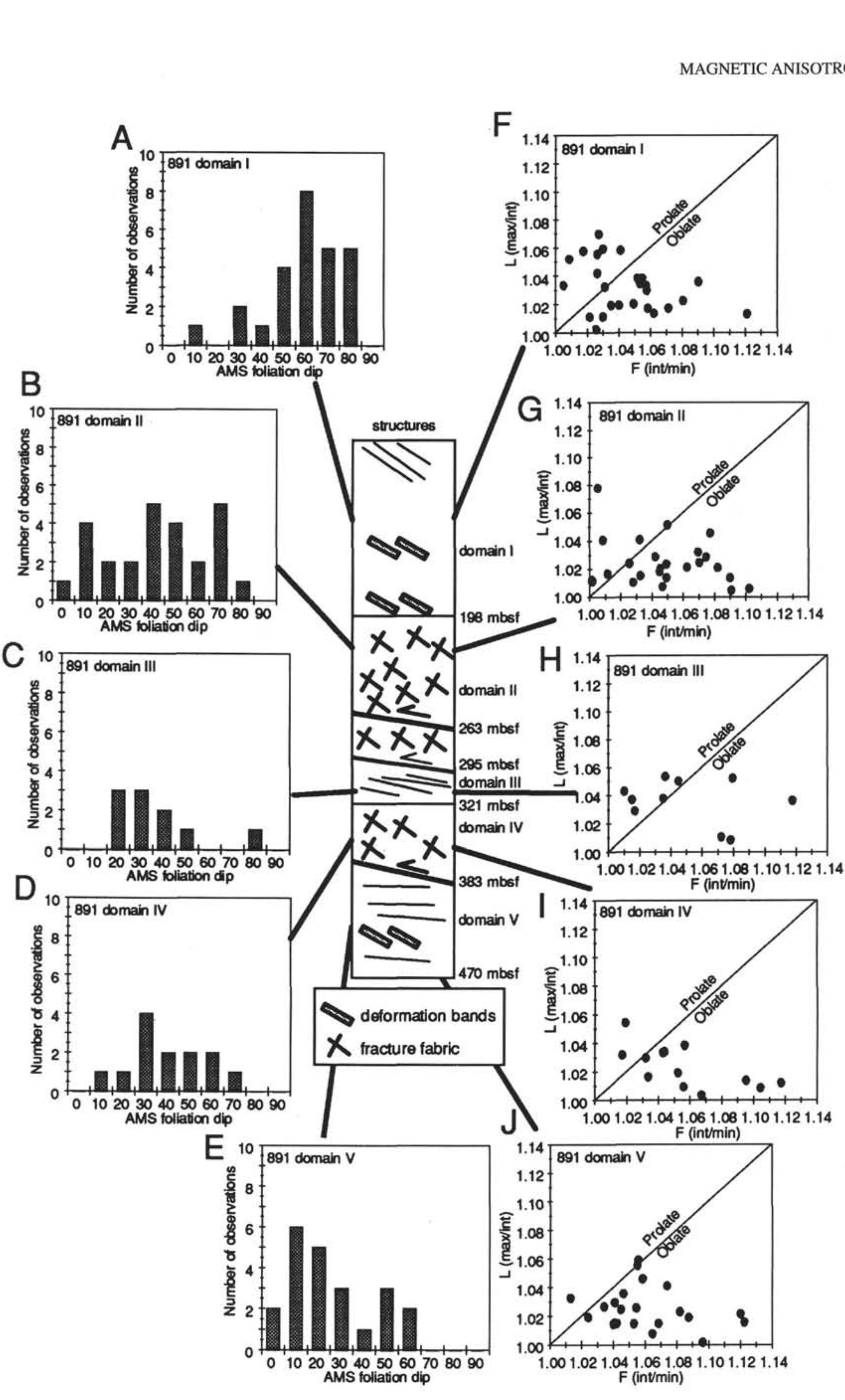

Figure 13. AMS results and schematic column of the principal structures (bedding, fracture fabrics, and deformation bands) and boundaries of the structural domains of Site 891. **A–E.** Orientations of the AMS fabrics are plotted as histograms of AMS foliation dips for each structural domain. The AMS foliation dips are defined as 90° (inclination of the minimum axis) for each sample, and represent the dips of the dominant planar fabric measured by AMS in these samples. **F–J.** Shapes of the AMS ellipsoids given as Flinn-type diagrams, as in Figure 5.

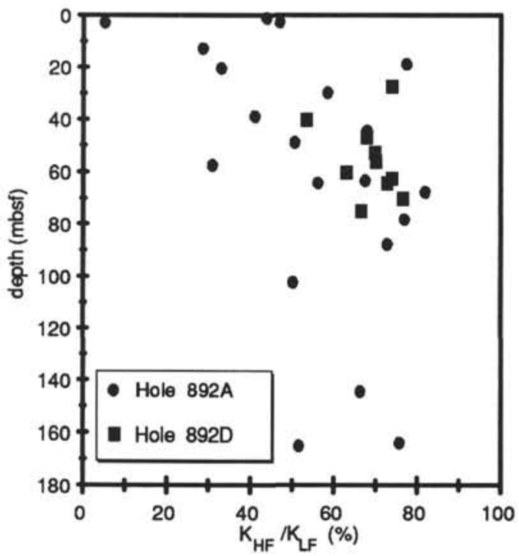

Figure 14. Depth (mbsf) vs. the percentage of low-field magnetic susceptibility carried by the paramagnetic minerals in sediments from Site 892, as determined by comparing the high-field and low-field susceptibilities. The proportion of the low-field susceptibility carried by the paramagnetic minerals varies from >80% to <10%, with most values ranging from 60% to 80%.

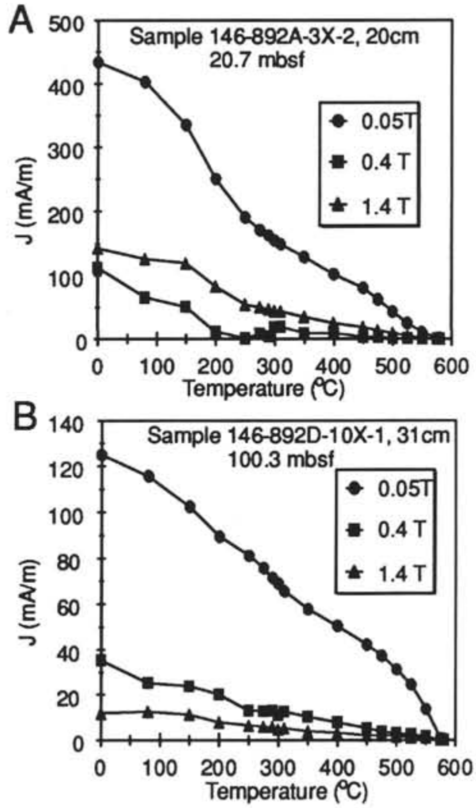

Figure 15. Thermal demagnetization of mIRM results for representative Site 892 samples. The vertical axes are magnetization of the mIRM components (mA/m), and the horizontal axes are temperature of the thermal demagnetization step. **A.** Sample dominated by the 0.05 T component, with two thermal unblocking temperatures (T_{ub}), one at about 300°C, and the other at about 580°C. This indicates that both greigite and/or pyrrhotite (T_{ub} ~300°C) and magnetite (T_{ub} ~580°C) are the dominant magnetic minerals in this sample. **B.** Sample dominated by the 0.05 T component, which is carried almost entirely by magnetite, indicated by the 590°C thermal unblocking temperature of this component.

Table 5. Anisotropy of magnetic susceptibility (AMS) data for Site 892.

Core, section, interval (cm)	Depth (mbsf)	K_{max} Dec	K_{max} Inc	K_{int} Dec	K_{int} Inc	K_{min} Dec	K_{min} Inc	K_{max} (1×10^{-6})	K_{int} (1×10^{-6})	K_{min} (1×10^{-6})	K_{mean} (1×10^{-6})	L	F	P	AMS dip
146-892A-															
1X-1, 15	0.2	101	18	192	3	292	71	88.8	88.5	86.7	88.0	1.00	1.02	1.02	19
1X-1, 105	1.1	38	2	308	14	137	76	95.4	94.9	93.3	94.5	1.01	1.02	1.02	15
1X-1, 130	1.3	93	5	3	1	266	85	76.5	76.0	75.5	76.0	1.01	1.01	1.01	5
1X-2, 41	1.9	29	30	151	43	277	33	117.8	117.4	116.7	117.3	1.00	1.01	1.01	57
1X-2, 96	2.5	234	15	330	21	112	64	74.7	74.0	73.3	74.0	1.01	1.01	1.02	26
1X-2, 99	2.5	225	1	316	12	128	78	108.8	108.1	107.4	108.1	1.01	1.01	1.01	12
1X-2, 137	2.9	266	13	174	7	56	75	73.7	73.2	72.1	73.0	1.01	1.01	1.02	15
1X-3, 11	3.1	291	53	39	12	136	34	711.0	701.1	624.8	679.0	1.01	1.12	1.14	56
1X-3, 37	3.3	204	17	108	19	332	64	116.6	116.1	115.6	116.1	1.00	1.00	1.01	26
2X-3, 48	13.0	86	7	177	6	306	81	88.6	88.3	87.8	88.2	1.00	1.01	1.01	9
2X-3, 54	13.0	48	26	184	56	307	20	163.7	163.1	141.2	156.0	1.00	1.15	1.16	70
3X-1, 8	19.1	231	25	344	39	117	40	47.3	47.0	46.7	47.0	1.01	1.01	1.01	50
3X-1, 54	19.5	108	15	200	7	315	74	107.3	106.6	104.7	106.2	1.01	1.02	1.02	17
3X-1, 109	20.1	82	4	352	0	254	85	102.7	101.3	98.7	100.9	1.01	1.03	1.04	5
3X-1, 119	20.2	146	6	56	11	262	77	63.7	63.1	62.3	63.0	1.01	1.01	1.02	13
3X-2, 20	20.7	93	20	220	59	354	23	104.1	102.8	102.1	103.0	1.01	1.01	1.02	67
3X-2, 34	20.8	250	4	341	15	142	74	102.9	101.5	100.5	101.6	1.01	1.01	1.02	16
3X-2, 90	21.4	73	39	208	41	322	24	60.5	60.3	59.1	60.0	1.00	1.02	1.02	66
3X-3, 22	22.0	331	0	241	2	71	88	64.8	64.6	62.6	64.0	1.00	1.03	1.04	2
3X-3, 57	22.4	269	5	359	4	127	83	150.3	149.8	147.8	149.3	1.00	1.01	1.02	7
3X-3, 84	22.6	180	7	276	38	82	51	60.8	60.2	59.0	60.0	1.01	1.02	1.03	39
4X-1, 52	29.0	20	6	111	5	240	82	116	116	111.8	114.6	1.00	1.04	1.04	8
4X-1, 94	29.4	171	20	42	60	269	21	60.3	60.1	59.7	60.0	1.00	1.01	1.01	69
4X-2, 52	30.0	78	4	168	1	276	85	51	50.6	48.8	50.1	1.01	1.04	1.05	5
4X-2, 54	30.1	281	15	189	9	68	72	26.3	26.1	25.6	26.0	1.01	1.02	1.03	18
4X-CC, 8	30.3	301	79	89	9	179	6	34.8	34.5	32.8	34.0	1.01	1.05	1.06	84
6X-1, 24	39.2	246	14	145	37	353	49	46.4	46.0	45.6	46.0	1.01	1.01	1.02	41
6X-1, 32	39.3	117	38	214	9	315	51	79.8	79	78.7	79.2	1.01	1.00	1.01	39
6X-1, 120	40.2	45	29	312	5	212	61	111.2	110.6	109.1	110.3	1.01	1.01	1.02	29
6X-2, 58	41.1	142	3	51	10	248	80	61.9	61.5	60.1	61.2	1.01	1.02	1.03	11
6X-2, 116	41.7	84	15	347	25	201	60	44.4	44.1	43.6	44.0	1.01	1.01	1.02	30
6X-2, 120	41.7	273	12	3	2	102	78	90	89.7	88.7	89.5	1.00	1.01	1.01	13
6X-3, 18	42.2	230	7	340	68	137	20	79.8	79.4	78.6	79.3	1.01	1.01	1.02	70
6X-3, 23	42.3	183	14	93	3	350	75	49.4	49.2	48.4	49.0	1.01	1.02	1.02	15
6X-4, 22	43.7	271	32	180	2	85	58	112.6	111.6	111.2	111.8	1.01	1.00	1.01	32
6X-4, 116	44.7	89	14	183	15	318	69	59.7	59	58.4	59.0	1.01	1.01	1.02	21
6X-4, 126	44.8	207	3	299	24	110	65	38.5	38.0	37.5	38.0	1.01	1.01	1.03	25
6X-5, 11	45.2	86	25	353	6	250	64	56.5	56.1	54.9	55.8	1.01	1.02	1.03	26
6X-5, 17	45.2	150	21	260	43	41	40	35.4	35.0	34.6	35.0	1.01	1.01	1.02	50
7X-1, 10	48.6	67	14	157	1	251	76	66.2	65.7	64.2	65.4	1.01	1.02	1.03	14
7X-1, 56	49.1	121	7	27	28	223	61	65.8	65.0	64.2	65.0	1.01	1.01	1.03	29
7X-2, 26	50.3	345	3	254	12	90	78	63.8	63.3	62.0	63.0	1.01	1.02	1.03	12
7X-2, 115	51.2	90	22	355	14	234	64	143.5	141.8	140.1	141.8	1.01	1.01	1.02	26
7X-2, 122	51.2	309	1	40	39	218	51	88.2	87.2	85.7	87.0	1.01	1.02	1.03	39
7X-3, 45	52.0	62	20	325	20	193	61	142.3	140.4	138.2	140.3	1.01	1.02	1.03	29
7X-3, 124	52.8	140	20	236	16	1	64	102.6	102.3	101.1	102.0	1.00	1.01	1.01	26
7X-3, 138	52.9	78	22	346	5	243	68	141.4	140.3	139.5	140.4	1.01	1.01	1.01	22
7X-4, 26	53.3	10	1	279	50	100	40	89.6	87.8	86.6	88.0	1.02	1.01	1.03	51
7X-4, 44	53.5	66	16	336	0	244	74	156	154.1	148.7	152.9	1.01	1.04	1.05	16
7X-4, 114	54.2	46	18	315	4	211	72	144.2	143.1	139.6	142.3	1.01	1.03	1.03	18
7X-6, 23	56.3	153	6	244	5	14	82	132.7	132.3	127.9	131.0	1.00	1.03	1.04	8
7X-6, 37	56.4	106	25	12	7	267	64	129.8	129.6	127	128.8	1.00	1.02	1.02	26
7X-6, 107	57.1	152	2	243	11	47	79	111.6	111	109.2	110.6	1.01	1.02	1.02	11
7X-6, 117	57.2	145	7	52	25	249	64	69.0	68.7	66.4	68.0	1.00	1.03	1.04	26
7X-7, 7	57.6	17	5	118	62	284	27	116.7	116	113.8	115.5	1.01	1.02	1.03	63
7X-7, 17	57.7	327	6	237	0	144	84	113.3	111.8	110.8	112.0	1.01	1.01	1.02	6
8X-1, 23	58.2	72	13	169	32	322	55	112.5	111.5	109.0	111.0	1.01	1.02	1.03	35
8X-1, 58	58.6	344	2	83	75	253	15	153.3	152	151.1	152.1	1.01	1.01	1.01	75
8X-1, 140	59.4	94	27	350	26	222	51	152.7	150.1	149.6	150.8	1.02	1.00	1.02	40
8X-2, 41	59.9	208	6	90	77	298	12	124.5	123.6	122.1	123.4	1.01	1.01	1.02	78
8X-3, 46	61.5	268	24	4	14	121	62	68.7	68.1	67.2	68.0	1.01	1.01	1.02	28
8X-3, 68	61.7	73	18	168	13	292	68	117.1	115.9	111.4	114.8	1.01	1.04	1.05	22
8X-3, 137	62.4	319	62	149	27	58	4	91.3	91.2	90.5	91.0	1.00	1.01	1.01	86
8X-3, 140	62.4	112	33	222	28	342	44	130.7	129.6	128.9	129.7	1.01	1.01	1.01	46
8X-4, 49	62.9	185	28	88	15	333	58	87.6	87.2	86.2	87.0	1.00	1.01	1.02	33
8X-4, 53	63.0	96	30	201	23	321	51	139.2	137.6	134.5	137.1	1.01	1.02	1.03	39
8X-4, 119	63.6	132	71	224	0	314	19	77.7	77	76	76.9	1.01	1.01	1.02	71
8X-4, 124	63.7	52	21	157	34	296	48	37.3	36.9	36.8	37.0	1.01	1.00	1.01	42
8X-5, 16	64.1	57	10	326	8	198	77	78.3	77.6	76.3	77.4	1.01	1.02	1.03	13
8X-5, 54	64.5	103	15	195	5	303	74	57.9	57.2	56.0	57.0	1.01	1.02	1.03	16
9X-1, 40	67.9	93	4	3	4	223	84	168.6	167.7	163.8	166.7	1.01	1.02	1.03	6
9X-1, 47	68.0	263	19	142	56	4	27	48.4	48.1	47.6	48.0	1.01	1.01	1.02	64
11X-1, 40	78.4	232	3	141	6	346	84	65.6	65.4	64.0	65.0	1.00	1.02	1.03	6
11X-1, 125	79.3	72	21	165	7	273	68	149.2	147.9	143.9	147.0	1.01	1.03	1.04	22
11X-2, 29	79.8	31	16	130	25	272	60	158.4	157	155.3	156.9	1.01	1.01	1.02	30
11X-3, 40	80.9	70	6	161	8	302	80	136.7	134.4	130.9	134.0	1.02	1.03	1.04	10
11X-3, 43	80.9	248	25	121	52	352	26	89.4	87.6	86.9	88.0	1.02	1.01	1.03	64
12X-1, 50	88.0	48	17	142	14	269	68	75.9	74.7	74.3	75.0	1.02	1.01	1.02	22
12X-1, 53	88.0	95	14	4	3	258	76	136	134.8	132.7	134.5	1.01	1.02	1.02	14
12X-CC, 24	88.4	101	15	10	2	270	75	125	124	121.4	123.5	1.01	1.02	1.03	15
13X-1, 5	97.1	119	24	23	12	269	63	94.3	93.8	92	93.4	1.01	1.02	1.03	27
13X-2, 15	97.4	134	19	233	25	10	58	63.1	62.6	62.3	62.7	1.01	1.00	1.01	32
13X-2, 27	97.6	228	80	27	9	117	4	55.4	55.1	54.5	55.0	1.01	1.01	1.02	86
13X-2, 44	97.7	32	16	124	3	224	74	114.3	113.1	111.3	112.9	1.01	1.02	1.03	16
13X-3, 37	98.2	82	12	173	0	265	78	102.6	102.3	101.1	102.0	1.00	1.01	1.01	12
13X-3, 79	98.7	19	5	110	5	245	83	104	103.5	102.4	103.3	1.00	1.01	1.02	8

Table 5 (continued).

Core, section, interval (cm)	Depth (mbsf)	K_{max} Dec	K_{max} Inc	K_{int} Dec	K_{int} Inc	K_{min} Dec	K_{min} Inc	K_{max} (1×10^{-6})	K_{int} (1×10^{-6})	K_{min} (1×10^{-6})	K_{mean} (1×10^{-6})	L	F	P	AMS dip
13X-4, 42	99.2	149	11	59	3	311	79	67.4	67.2	66.4	67.0	1.00	1.01	1.01	11
13X-4, 45	99.2	25	12	118	10	247	74	102.1	101.7	100.7	101.5	1.00	1.01	1.01	16
13X-5, 16	100.3	81	29	196	37	324	39	52.4	51.8	51.8	52.0	1.01	1.00	1.01	51
13X-5, 61	100.7	90	15	190	34	339	52	52.4	52.1	51.5	52.0	1.01	1.01	1.02	38
13X-5, 63	100.7	43	12	138	18	281	68	110.7	109.8	108.9	109.8	1.01	1.01	1.02	22
13X-6, 19	101.1	260	13	22	67	165	19	92.7	92.3	91.7	92.2	1.00	1.01	1.01	71
13X-7, 55	102.5	126	12	216	2	313	77	75.3	74.3	72.4	74.0	1.01	1.03	1.04	13
13X-7, 112	103.1	104	11	196	10	327	75	90.1	89.4	87.5	89.0	1.01	1.02	1.03	15
13X-8, 9	103.5	34	8	126	11	265	76	139.3	137.4	134.9	137.2	1.01	1.02	1.03	14
13X-8, 54	104.0	71	21	337	10	224	66	60.8	60.3	59.0	60.0	1.01	1.02	1.03	24
13X-8, 96	104.4	66	26	168	24	295	54	114.9	113.5	112.7	113.7	1.01	1.01	1.02	37
13X-9, 49	105.3	100	29	203	21	324	53	99.6	98.4	97.2	98.4	1.01	1.01	1.02	37
13X-9, 102	105.8	88	24	356	6	251	65	105.6	104.8	104	104.8	1.01	1.01	1.02	25
15X-1, 37	116.4	143	17	239	20	16	64	89.2	88.8	86.0	88.0	1.01	1.03	1.04	26
15X-1, 39	116.4	166	25	72	8	325	64	126.4	125.8	124.3	125.5	1.00	1.01	1.02	26
15X-1, 54	116.5	156	8	65	6	299	80	81.1	80.5	78.4	80.0	1.01	1.03	1.04	10
15X-1, 59	116.6	109	3	200	29	13	61	122	121.6	118.8	120.8	1.00	1.02	1.03	29
16X-1, 18	125.7	115	4	207	23	17	66	65.6	65.1	64.3	65.0	1.01	1.01	1.02	24
16X-CC, 13	126.1	64	6	157	23	318	66	86.7	86.2	85.9	86.3	1.01	1.00	1.01	25
17X-1, 37	135.4	114	0	204	5	18	85	82.3	81.5	80.4	81.4	1.01	1.01	1.02	5
17X-2, 22	135.8	79	10	172	17	319	70	67.3	66.9	66	66.7	1.01	1.01	1.02	20
18X-1, 17	144.7	118	10	29	0	297	80	79.1	78.4	76.5	78.0	1.01	1.02	1.03	10
18X-1, 38	144.9	236	2	328	46	143	44	117.7	115.7	111.6	115.0	1.02	1.04	1.05	46
18X-1, 85	145.4	168	12	78	4	332	78	112.3	110.3	104.4	109.0	1.02	1.06	1.08	12
18X-CC, 1	146.4	9	7	274	36	109	53	310.7	295.9	289.5	298.7	1.05	1.02	1.07	37
20X-1, 49	164.0	243	0	333	12	149	78	167.1	165.8	163.8	165.6	1.01	1.01	1.02	12
20X-1, 69	164.2	288	4	195	32	25	57	82.6	82.1	81.3	82.0	1.01	1.01	1.02	33
20X-1, 116	164.7	98	6	191	22	352	67	120.1	118.4	113.4	117.3	1.01	1.04	1.06	23
20X-2, 22	165.2	116	14	206	1	300	76	88.1	87.1	85.7	87.0	1.01	1.02	1.03	14
20X-2, 28	165.3	216	4	122	44	310	45	132.2	131	129.2	130.8	1.01	1.01	1.02	45
20X-2, 109	166.1	300	4	31	10	190	79	89.9	89.3	87.8	89.0	1.01	1.02	1.02	11
20X-2, 126	166.3	37	10	129	4	241	79	125.8	125	121.5	124.1	1.01	1.03	1.04	11
20X-2, 141	166.4	113	13	22	7	263	75	75.8	75.0	74.2	75.0	1.01	1.01	1.02	15
20X-CC, 22	167.3	104	1	194	10	4	80	137.6	136.6	133	135.7	1.01	1.03	1.03	11
146-892D-															
4X-1, 33	27.8	108	16	203	19	341	65	63.7	63.0	62.3	63.0	1.01	1.01	1.02	25
4X-2, 42	29.4	42	13	137	17	277	68	62.8	62.4	62	62.4	1.01	1.01	1.01	22
4X-3, 40	30.4	50	5	140	7	283	81	77.1	76.8	74.0	76.0	1.00	1.04	1.04	9
4X-3, 77	30.8	52	7	144	9	284	78	115	113.9	112.9	113.9	1.01	1.01	1.02	12
5X-1, 42	37.4	32	22	300	3	204	68	89.9	89.1	87.9	89.0	1.01	1.01	1.02	22
5X-1, 90	37.9	297	9	200	41	37	48	169.5	168.9	168.6	169.0	1.00	1.00	1.01	42
5X-2, 24	38.7	134	7	42	8	262	79	76.2	75.8	74.8	75.6	1.01	1.01	1.02	11
5X-3, 12	40.1	103	36	346	33	226	38	66.4	65.4	65	65.6	1.02	1.01	1.02	53
5X-3, 54	40.5	162	12	275	61	66	26	46.4	46.0	45.6	46.0	1.01	1.01	1.02	64
5X-4, 28	41.8	23	15	283	33	133	53	55.5	55.0	54.5	55.0	1.01	1.01	1.02	37
5X-4, 67	42.2	64	22	159	9	270	66	97	96.1	95.1	96.1	1.01	1.01	1.02	24
6X-1, 66	47.2	96	4	5	11	207	78	54.3	54.2	53.5	54.0	1.00	1.01	1.02	12
6X-1, 126	47.8	65	9	331	21	177	67	68.6	68.0	67.3	68.0	1.01	1.01	1.02	23
6X-1, 148	48.0	75	2	166	18	338	72	103	102.4	101.8	102.4	1.01	1.01	1.01	18
6X-2, 19	48.2	84	22	352	7	244	67	69.8	68.9	67.8	68.8	1.01	1.02	1.03	23
6X-3, 48	49.7	127	1	219	60	36	30	81.5	80.9	80.6	81.0	1.01	1.00	1.01	60
6X-3, 79	50.0	360	2	90	7	252	82	138	138.1	136.9	137.7	1.00	1.01	1.01	8
6X-4, 124	52.0	113	8	22	3	270	81	37.6	37.4	36.9	37.3	1.01	1.01	1.02	9
6X-4, 125	52.0	3	3	93	16	263	74	39.3	39.2	38.5	39.0	1.00	1.02	1.02	16
6X-5, 94	53.2	110	19	203	7	313	70	49.4	49.4	48.2	49.0	1.00	1.02	1.02	20
7X-1, 27	54.3	115	22	353	52	218	29	41.7	40.9	40.4	41.0	1.02	1.01	1.03	61
7X-1, 76	54.8	138	24	231	6	333	65	76	75.2	74.2	75.1	1.01	1.01	1.02	25
7X-2, 95	56.5	150	21	260	42	40	41	50.3	49.9	49	49.7	1.01	1.02	1.03	49
7X-2, 103	56.5	75	11	168	14	308	71	42.5	41.9	41.7	42.0	1.01	1.00	1.02	19
7X-3, 20	57.0	103	26	1	24	234	53	44.6	44.1	43.3	44.0	1.01	1.02	1.03	37
7X-3, 114	57.9	87	28	181	8	286	61	53.4	53.0	52.5	53.0	1.01	1.01	1.02	29
7X-3, 128	58.0	55	22	150	12	267	65	104	102.7	100.3	102.3	1.01	1.02	1.04	25
7X-4, 31	58.6	162	21	255	8	6	68	46.6	46.1	45.3	46.0	1.01	1.02	1.03	23
7X-4, 102	59.3	96	4	0	53	190	37	63.4	62.7	62.2	62.8	1.01	1.01	1.02	54
7X-5, 63	60.4	36	16	130	13	256	69	86.5	86.1	84.1	85.6	1.00	1.02	1.03	21
7X-5, 79	60.6	166	35	264	11	10	53	45.5	45.2	44.3	45.0	1.01	1.02	1.03	37
8X-1, 22	61.9	35	38	301	4	207	51	66.8	65.8	65.4	66.0	1.01	1.01	1.02	39
8X-1, 51	62.2	341	17	78	24	218	60	121	120	117.4	119.5	1.01	1.02	1.03	30
8X-1, 120	62.9	111	5	21	3	266	84	19.3	19.2	18.5	19.0	1.01	1.03	1.04	6
8X-2, 19	63.2	66	7	334	15	179	73	65.6	65.1	64.4	65.0	1.01	1.01	1.02	17
8X-2, 61	63.6	202	10	109	14	325	73	85.0	84.8	82.2	84.0	1.00	1.03	1.03	18
8X-2, 69	63.7	49	17	149	29	292	56	144	143	140.8	142.6	1.01	1.02	1.02	34
8X-3, 16	64.7	69	18	163	12	285	68	69.7	69.1	68.2	69.0	1.01	1.01	1.02	22
8X-3, 32	64.8	93	14	1	5	252	75	134	132.7	130.2	132.3	1.01	1.02	1.03	15
8X-3, 121	65.7	343	32	76	4	173	58	72.8	71.9	71.2	72.0	1.01	1.01	1.02	32
8X-4, 26	66.4	341	3	73	29	245	60	153	152.1	150.2	151.8	1.01	1.01	1.02	30
9X-1, 41	69.7	233	49	11	33	116	22	101	99.7	99.4	100.0	1.01	1.00	1.02	68
9X-1, 122	70.5	116	15	208	9	327	73	92.6	91.8	88.6	91.0	1.01	1.04	1.05	17
9X-2, 50	71.3	227	33	348	39	110	34	111	109.1	105.1	108.4	1.02	1.04	1.06	56
9X-2, 57	71.4	142	19	241	24	18	59	73.7	72.5	69.8	72.0	1.02	1.04	1.06	31
9X-3, 33	71.9	180	38	294	28	50	39	76.5	76.2	75.3	76.0	1.00	1.01	1.02	51
9X-4, 72	73.3	105	20	13	5	267	69	79.6	79.2	78.3	79.0	1.01	1.01	1.02	21
9X-4, 85	73.4	95	32	191	10	296	57	84.7	84.2	83.1	84.0	1.01	1.01	1.02	34
9X-5, 29	73.8	69	20	158	0	250	70	71.7	71.3	70.0	71.0	1.00	1.02	1.02	20
9X-5, 74	74.3	97	17	203	40	350	45	66.2	65.4	65.2	65.6	1.01	1.00	1.02	45
9X-6, 33	75.2	193	4	102	18	296	72	91.2	91.1	89.3	90.5	1.00	1.02	1.02	18
9X-6, 37	75.2	50	5	142	34	312	55	80.4	79.6	77.0	79.0	1.01	1.03	1.04	35

Table 5 (continued).

Core, section, interval (cm)	Depth (mbsf)	K_{max} Dec	K_{max} Inc	K_{int} Dec	K_{int} Inc	K_{min} Dec	K_{min} Inc	K_{max} (1×10^{-6})	K_{int} (1×10^{-6})	K_{min} (1×10^{-6})	K_{mean} (1×10^{-6})	L	F	P	AMS dip
9X-CC, 14	75.5	148	8	56	16	263	72	62.6	62.4	60.9	62.0	1.00	1.02	1.03	18
9X-CC, 28	75.6	110	3	201	27	13	63	77.1	76.3	73.9	75.8	1.01	1.03	1.04	28
10X-1, 2	100.0	305	18	38	10	156	69	102	102	101.6	101.9	1.00	1.00	1.00	21
10X-1, 31	100.3	203	19	111	6	5	70	118.0	117.1	112.9	116.0	1.01	1.04	1.04	20
10X-2, 27	101.0	135	49	35	8	297	40	167	165.2	160.9	164.4	1.01	1.03	1.04	50
10X-2, 29	101.0	138	32	37	19	281	52	108.7	107.2	105.1	107.0	1.01	1.02	1.03	38
10X-3, 6	102.3	113	49	13	8	276	40	141	139.9	138.5	139.8	1.01	1.01	1.02	50
10X-3, 8	102.3	118	35	17	15	267	51	89.3	88.0	86.7	88.0	1.02	1.01	1.03	39
10X-4, 105	104.8	349	18	252	21	116	61	68.8	68.1	67.1	68.0	1.01	1.02	1.02	29
10X-4, 138	105.1	260	66	170	0	79	24	161	158.5	156.7	158.7	1.02	1.01	1.03	66
10X-5, 40	105.7	192	37	100	3	8	53	69.7	69.6	67.7	69.0	1.00	1.03	1.03	37
10X-6, 21	106.5	14	44	280	4	185	45	138	138	133.6	136.5	1.00	1.03	1.03	45
10X-6, 53	106.9	279	54	16	5	109	36	90.7	89.0	87.3	89.0	1.02	1.02	1.04	54
10X-7, 31	108.1	5	50	258	14	157	36	137	135.2	134.3	135.5	1.01	1.01	1.02	54
10X-7, 134	109.2	292	65	185	7	93	24	96.2	95.7	93.1	95.0	1.01	1.03	1.03	67
10X-8 54	109.9	97	12	191	16	331	70	124	122.8	119.7	122.2	1.01	1.03	1.04	21
11X-1, 71	110.2	293	1	202	12	26	78	87.9	87.8	85.3	87.0	1.00	1.03	1.03	12
10X-CC, 19	110.5	276	22	173	30	37	52	115	114.3	108.6	112.6	1.01	1.05	1.06	39
11X-2, 132	112.3	124	17	214	1	307	73	91.9	91.8	86.3	90.0	1.00	1.06	1.07	17
11X-2, 145	112.5	69	16	160	4	264	74	133	130.7	127.7	130.5	1.02	1.02	1.04	17
11X-3, 1	112.5	69	21	177	37	316	45	132	130.2	128.2	130.1	1.01	1.02	1.03	45
11X-3, 4	112.5	113	8	206	16	359	72	92.3	91.7	89.0	91.0	1.01	1.03	1.04	18
11X-CC, 17	112.9	67	46	171	13	272	42	175	173.4	169.9	172.8	1.01	1.02	1.03	48
12X-1, 59	119.6	70	43	194	32	305	31	67.4	66.9	66.7	67.0	1.01	1.00	1.01	59
12X-2, 31	120.8	296	10	201	29	44	60	85.6	84.2	82.2	84.0	1.02	1.02	1.04	30
12X-2, 34	120.8	54	6	145	2	253	83	121	121.2	117.3	119.8	1.00	1.03	1.03	7
12X-3, 76	122.8	38	5	130	13	287	76	119	118.1	116.2	117.8	1.01	1.02	1.02	14
12X-3, 96	123.0	25	12	286	36	131	52	103.8	102.5	99.7	102.0	1.01	1.03	1.04	38
12X-4, 21	123.7	249	58	49	30	144	9	65.4	65.1	64.5	65.0	1.00	1.01	1.01	81
12X-4, 43	123.9	71	11	169	32	325	56	81.7	81.5	80.9	81.4	1.00	1.01	1.01	34
12X-4, 99	124.5	94	12	3	1	267	78	64.8	64.1	63.1	64.0	1.01	1.02	1.03	12
14X-CC, 3	139.8	92	16	185	6	295	73	104	103.4	101.2	102.9	1.01	1.02	1.03	17
15X-1, 77	148.3	76	16	343	9	226	72	86.1	85.3	83.6	85.0	1.01	1.02	1.03	18
15X-1, 95	148.5	80	18	175	14	300	67	155	153.8	150.6	153.1	1.01	1.02	1.03	23
15X-2, 75	149.8	114	10	204	2	307	80	157	155.9	152.7	155.2	1.01	1.02	1.03	10
15X-2, 78	149.8	97	5	7	4	239	84	77.9	77.6	75.6	77.0	1.00	1.03	1.03	6
15X-3, 24	150.7	35	6	300	35	132	55	69.0	68.6	66.3	68.0	1.01	1.03	1.04	35
15X-3, 59	151.1	68	3	158	8	315	81	219.4	215.0	204.6	213.0	1.02	1.05	1.07	9
15X-3, 81	151.3	73	9	341	12	201	75	80.0	79.3	77.7	79.0	1.01	1.02	1.03	15
15X-3, 145	152.0	24	20	124	25	261	57	109	108.1	107.6	108.2	1.01	1.00	1.01	33
15X-CC, 5	152.2	122	15	26	17	249	67	121	120.2	119.3	120.2	1.01	1.01	1.01	23
16X-1, 41	157.4	78	36	334	19	221	48	117	116.1	114.8	116.0	1.01	1.01	1.02	42
16X-2, 5	158.1	19	11	111	7	234	77	89.5	88.8	87.3	88.5	1.01	1.02	1.03	13
16X-3, 25	159.8	46	5	135	4	265	84	80.8	80.7	78.5	80.0	1.00	1.03	1.03	6
16X-4, 24	161.3	150	33	47	19	292	51	45.6	45.0	44.4	45.0	1.01	1.01	1.03	39
16X-5, 127	163.8	297	3	206	10	44	79	79	78.7	76.5	78.1	1.00	1.03	1.03	11
16X-5, 128	163.8	106	30	199	4	296	59	46.6	45.9	45.5	46.0	1.01	1.01	1.02	31
146-892E															
3H-1, 16	33.2	92	7	186	37	353	52	35.5	35.2	34.4	35.0	1.01	1.02	1.03	38
3H-1, 95	34.0	299	20	185	50	42	34	47.6	47.3	46.2	47.0	1.01	1.02	1.03	56
3H-2, 2	34.2	57	8	321	41	157	48	59.3	58.6	58.3	58.7	1.01	1.01	1.02	42
3H-2, 7	34.2	198	10	291	13	72	73	29.4	29.1	28.5	29.0	1.01	1.02	1.03	17
3H-3, 74	35.9	191	49	329	33	74	22	28.4	28.0	27.7	28.0	1.01	1.01	1.02	68
3H-4, 52	37.2	329	10	228	48	68	40	21.3	21.1	20.7	21.0	1.01	1.02	1.03	50
3H-4, 120	37.8	188	10	279	6	41	79	78.7	78.3	77.0	78.0	1.00	1.02	1.02	12
3H-4, 128	37.9	190	6	281	5	52	81	91.4	91.1	90.2	90.9	1.00	1.01	1.01	9
3H-5, 9	38.2	77	18	306	63	174	19	38.8	38.5	37.8	38.4	1.01	1.02	1.03	71
3H-5, 65	38.8	67	0	157	70	336	20	44.6	43.9	43.5	44.0	1.02	1.01	1.03	70
3H-6, 41	40.0	243	36	146	9	44	52	55.6	55.4	54.0	55.0	1.00	1.03	1.03	38
3H-CC, 9	40.5	226	32	134	3	37	58	55.9	55.9	55.7	55.8	1.00	1.00	1.00	32
3H-CC, 25	40.6	82	6	191	73	350	16	48.5	47.8	47.7	48.0	1.02	1.00	1.02	74
4H-1, 45	43.0	219	21	129	0	39	69	85.1	84.2	82.7	84.0	1.01	1.02	1.03	21
4H-1, 51	43.0	81	42	204	31	316	32	97.4	96.6	95.8	96.6	1.01	1.01	1.02	58
4H-2, 42	44.2	61	5	155	46	326	44	46.4	46.1	45.5	46.0	1.01	1.01	1.02	47
4H-CC, 5	46.2	205	36	298	5	35	54	80.1	79.5	77.4	79.0	1.01	1.03	1.03	36
4H-CC, 16	46.3	219	20	123	16	356	64	132.1	131.1	129.5	130.9	1.01	1.01	1.02	26

Notes: Dec = declination (degrees); Inc = inclination (degrees); K_{max}, K_{int}, K_{min}, K_{mean} in SI volume units; L = K_{max}/K_{int}; F = K_{int}/K_{min}; P = K_{max}/K_{min}; AMS dip = (90 – K_{min} inc)

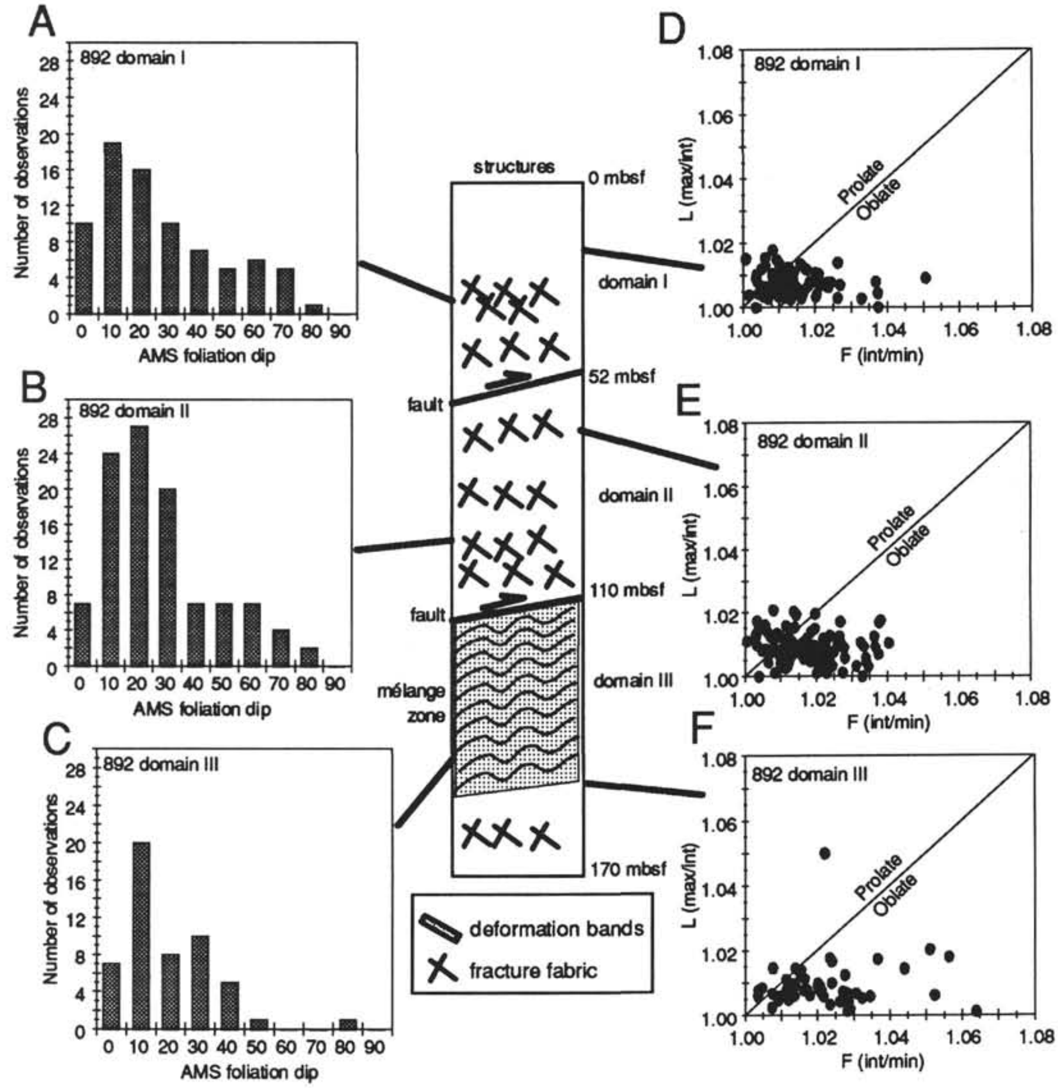

Figure 16. AMS results and schematic column of the principal structures (bedding, mélange, fracture fabrics, and deformation bands) and boundaries of the structural domains of Site 892. **A–C.** Orientations of the AMS fabrics are plotted as histograms of AMS foliation dips for each structural domain. The AMS foliation dips are defined as 90° (inclination of the minimum axis) for each sample, and represent the dips of the dominant planar fabric measured by AMS in these samples. **D–F.** Shapes of the AMS ellipsoids given as Flinn-type diagrams, as in Figure 5.

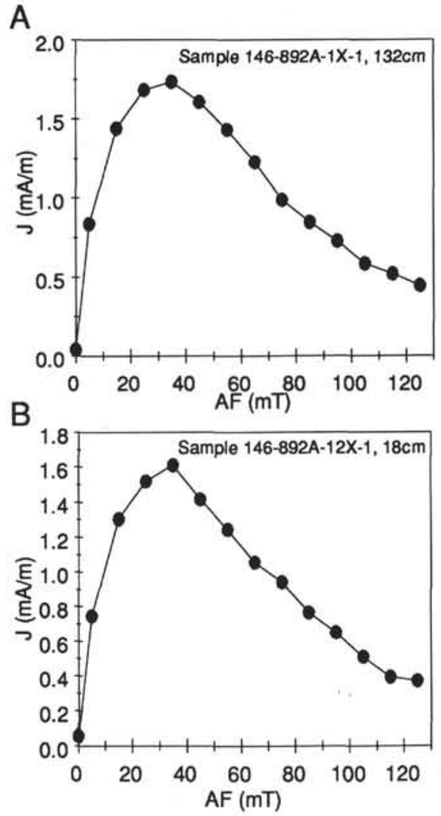

Figure 17. pARM curves for representative Site 892 samples. The vertical axis are magnetization (mA/m), and the horizontal axes are the intensities of the alternating field used to generate the pARM for each step. A 10-mT-wide window was used, and the center of the window was marked in increments of 10 mT from 5 to 155 mT. All samples have peak pARMs between 25 mT and 35 mT, with most of the pARM occurring between 5 mT and 60 mT.

Table 6. Anhysteretic remanent magnetization anistropy (ARMA) data for Site 892.

Core, section, interval (cm)	Depth (mbsf)	$pARM_{max}$		$pARM_{int}$		$pARM_{min}$		pARM (mA/m)				L	F	P	ARMA dip
		Dec	Inc	Dec	Inc	Dec	Inc	Max	Int	Min	Mean				
146-892A-															
1X-1, 132	1	232	22	140	4	39	67	8.1	8.0	7.7	7.9	1.01	1.04	1.05	23
3X-2, 59	21	127	0	37	11	218	79	12.4	12.14	11.68	12.1	1.02	1.04	1.06	11
4X-1, 59	29	121	11	212	3	315	79	9.18	8.58	8.18	8.6	1.07	1.05	1.12	11
6X-1, 44	39	205	14	112	13	340	71	7.74	7.57	7.29	7.5	1.02	1.04	1.06	19
7X-1, 42	49	328	1	237	5	73	85	9.17	8.93	8.49	8.9	1.03	1.05	1.08	5
7X-6, 80	57	119	18	22	20	247	63	12.02	11.91	11.48	11.8	1.01	1.04	1.05	27
8X-3, 53	62	138	6	48	2	301	84	14.61	14.04	13.65	14.1	1.04	1.03	1.07	6
11X-1, 90	79	57	19	321	17	192	65	9.08	9.04	8.76	9.0	1.00	1.03	1.04	25
12X-1, 18	88	190	26	287	13	42	61	7.88	7.82	7.36	7.7	1.01	1.06	1.07	29
13X-7, 64	103	133	20	43	0	313	70	9.41	9.06	8.71	9.1	1.04	1.04	1.08	20
17X-CC, 20	137	48	27	315	6	213	62	9.22	8.74	8.12	8.7	1.05	1.08	1.14	28
18X-1, 72	145	152	6	61	10	271	78	8.96	8.8	8.39	8.7	1.02	1.05	1.07	12
18X-CC, 3	146	331	3	240	17	71	73	19.2	18.62	17.21	18.3	1.03	1.08	1.12	17
146-892D-															
5X-1, 100	38	3	7	95	14	247	74	14.26	13.5	13.01	13.6	1.06	1.04	1.10	16
5X-3, 36	40	10	27	104	8	210	62	12.14	12	11.63	11.9	1.01	1.03	1.04	28
6X-1, 89	47	314	2	224	9	58	81	11.99	11.79	11.5	11.8	1.02	1.03	1.04	9

Notes: Dec = declination (degrees); Inc = inclination (degrees); Max, Int, Min, Mean = pARM in mA/m; L = max/int; F = int/min; P = max/min; ARMA dip = (90 - $pARM_{min}$ inc).

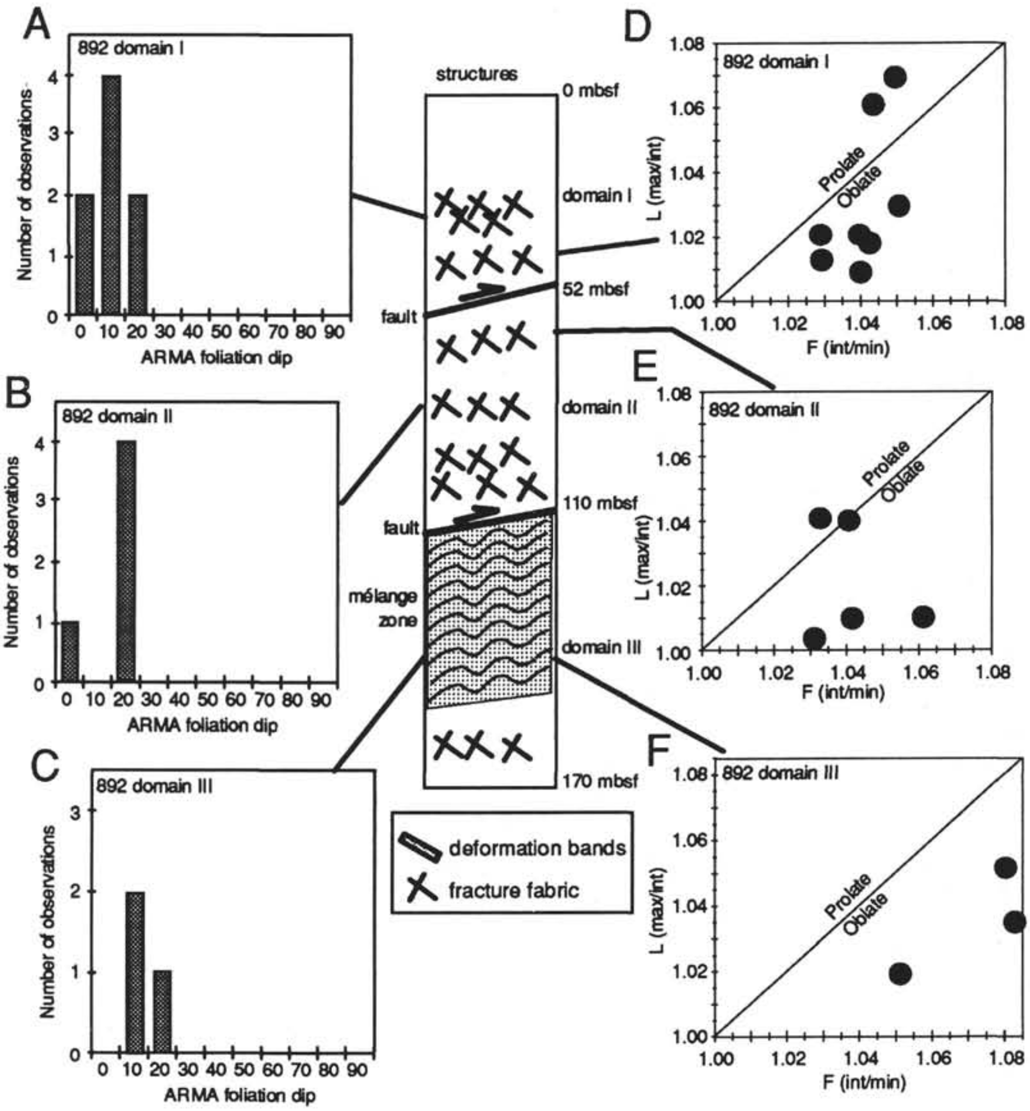

Figure 18. ARMA results for Site 892 samples. ARMA orientations (**A–C**) and ellipsoid shapes (**D–F**) are plotted for each structural domain as in Figure 16.